Journal of Volcanology and Geothermal Research xxx (2016) xxx–xxx

Contents lists available at ScienceDirect

Journal of Volcanology and Geothermal Research

journal homepage: www.elsevier.com/locate/jvolgeores

Mechanical behaviour of dacite from Mount St. Helens (USA): A link between porosity and lava dome extrusion mechanism (dome or spine)?

M.J. Heap [a,*], J.K. Russell [b], L.A. Kennedy [b]

[a] Géophysique Expérimentale, Institut de Physique de Globe de Strasbourg (IPGS), École et Observatoire des Sciences de la Terre (EOST), Université de Strasbourg (UMR 7516 CNRS), 5 rue René Descartes, 67084 Strasbourg, France
[b] Volcanology and Petrology Laboratory, Department of Earth and Ocean Sciences, University of British Columbia, 6339 Stores Road, Vancouver, V6T 1Z4, British Columbia, Canada

ARTICLE INFO

Article history:
Received 8 July 2016
Received in revised form 28 October 2016
Accepted 28 October 2016
Available online xxxx

Keywords:
Porosity
Permeability
Strength
Brittle
Ductile
Triaxial

ABSTRACT

There is a rich diversity in lava dome morphology, from blocky domes and lobes to imposing spine and whaleback structures. The latter extrude via seismically active, gouge-rich conduit-margin faults, a manifestation of a brittle failure mode. Brittle versus ductile behaviour in volcanic rocks is known to be porosity dependent, and therefore offers a tantalising link between the properties of the material near the conduit margin and the extrusion mechanism (dome or spine). We test this hypothesis by complementing published data on the mechanical behaviour of dacites from the 2004–2008 spine-forming eruption at Mount St. Helens (MSH) with new data on dacite lavas collected from the 1980 dome. The 1980 dacite samples were deformed at room temperature under a range of pressures (i.e., depths) to investigate their mechanical behaviour and failure mode (brittle or ductile). Low-porosity dacite (porosity ~0.19) is brittle up to an effective pressure of 30 MPa (depth ~1 km) and is ductile at 40 MPa (depth ~1.5 km). High-porosity dacite (porosity ~0.32) is ductile above an effective pressure of 5 MPa (depth ~200 m). Samples deformed in the brittle regime show well-developed (~1 mm) shear fracture zones comprising broken glass and crystal fragments. Samples deformed in the ductile regime feature anastomosing bands of collapsed pores. The combined dataset is used to explore the influence of strain rate, temperature, and porosity on the mechanical behaviour and failure mode of dacite. A decrease in strain rate does not influence the strength of dacite at low temperature, but reduces strength at high temperature (850 °C). Due to the extremely low glass content of these materials, such weakening is attributed to the increased efficiency of subcritical crack growth at high temperature. However, when strain rate is kept constant, temperature does not significant impact strength reflecting the highly crystallised nature of dacite from MSH. Dacite from the 2004–2008 eruption is stronger than 1980 dome material and remains brittle even at high effective pressures, a consequence of their low preserved porosities. Only the porous (porosity ~0.32) 1980 dome material deformed in a ductile manner (i.e., no macroscopic shear fracture) at effective pressures relevant for edifice deformation. Spine formation typically involves the extrusion of low-porosity material along faults that envelop the magma-filled conduit (i.e., brittle deformation), suggesting that the extrusion mechanism (dome or spine) may be a consequence of slow ascent rates and efficient pre-eruptive outgassing. Well-outgassed, low-porosity (slow ascent rate) materials favour a brittle mode of failure promoting spine extrusion, while poorly-outgassed, high-porosity (fast ascent rate) materials result in blocky domes or lobes. A crystal content-porosity map for brittle (spine) versus ductile (blocky dome) behaviour demonstrates that the window for brittle deformation is small and offers an explanation as to why spine and whaleback structures are relatively rare in nature.

1. Introduction

Lava dome morphology is richly diverse (Watts et al., 2002; Calder et al., 2015). Although most lava dome forming eruptions result in blocky domes and lobes, there are curious and spectacular instances of dense spines that extrude via seismically active, gouge-rich conduit-margin faults (e.g., Nakada et al., 1999; Watts et al., 2002; Melnik and Sparks, 2002; Iverson et al., 2006; Pallister et al., 2008; Cashman et al., 2008; Kennedy and Russell, 2012; Gaunt et al., 2014; Kendrick et al., 2014; Hornby et al., 2015; Lamb et al., 2015). Recent examples include the 1990–1995 activity at Mount Unzen (Kyūshū, Japan) that saw the growth of a spine over 40 m in height (Nakada et al., 1999), the growth of spines or "whalebacks" during the 2004–2008 eruptive activity at Mount St. Helens (MSH; Washington, USA) (Iverson et al., 2006), and the extrusion of "megaspines" during the 1996 activity at Soufrière Hills volcano (Montserrat) (Watts et al., 2002). The conduit-margin fractures at the conduit-wall rock interface are a manifestation of a

* Corresponding author.
E-mail address: heap@unistra.fr (M.J. Heap).

http://dx.doi.org/10.1016/j.jvolgeores.2016.10.015
0377-0273/© 2016 Elsevier B.V. All rights reserved.

brittle deformation mode. The porosity dependence of brittle versus ductile behaviour in volcanic rocks (Heap et al., 2015a; Zhu et al., 2016) therefore offers a tantalising link between extrusion mechanism (dome or spine) and the porosity of the material at the conduit-wall rock interface. While low-porosity volcanic rocks generally behave in a brittle manner at low and high pressure (or depth), high-porosity rocks can be brittle at low pressure and ductile at high pressure (or depth) (Heap et al., 2015a; Zhu et al., 2016).

The ability of ascending magma to outgas exsolving volatiles, and the time available for such outgassing, likely play key roles in the porosity present in magma and preserved in volcanic rock (e.g., Watts et al., 2002; Melnik and Sparks, 2002). Viewed simplistically, moderate to fast ascending magmas have little time for outgassing, cooling, and crystallisation. These magmas reach the surface as hot, high-porosity, melt-bubble mixtures with subordinate crystal contents; brittle behaviour in these lavas is therefore unlikely (we further note that an increase in the crystal content of magma increases the likelihood of brittle behaviour; Cordonnier et al., 2012). By contrast, slow ascending magmas have a greater opportunity to outgas, and allow more time for cooling to their appropriate glass transition temperature (*Tg*) and/or for crystallisation of the melt prior to extrusion (e.g., Cashman et al., 2008). The extruded materials in this case will be low-porosity, highly crystallised lava or lava that is near or below *Tg* and, as a result, brittle behaviour is more probable.

To explore the porosity dependence of the extrusion mechanism—dome or spine—we complement pre-existing data on the physical properties (e.g., porosity and permeability) and mechanical behaviour of dacites from the 2004–2008 spine-forming eruption at MSH (Klug and Cashman, 1996; Kennedy et al., 2009; Smith et al., 2011; Kennedy and Russell, 2012; Kendrick et al., 2013; Gaunt et al., 2014, 2016) with new data on dacite lavas collected from the 1980 dome. We first characterised our samples in terms of their textural properties, porosity, permeability, and their porosity-permeability relationship. We then present results from room temperature triaxial experiments performed at different effective pressures (depths) in which we monitored porosity change and the output of acoustic emission energy during deformation. Post-deformation microstructural analysis was employed to understand the micromechanisms of deformation. The data compilation (i.e., published data from 2004–2008 spine-forming dacites and new data from 1980 dome-forming dacites) is used to explore porosity-permeability relationships and the range of mechanical behaviour and failure modes (brittle or ductile) to be expected of dacite as a function of its residual porosity, strain rate, and temperature. We use insight gleaned from these data to map out porosity-crystal (or glass/melt) content windows for spine versus blocky lava dome extrusion. We further anticipate that the physical and mechanical data compiled here will inform models of slope stability and outgassing at MSH and at other active dacitic volcanoes worldwide.

2. Mount St. Helens (MSH), Washington (USA)

Our principal goal is to present data that can inform on mechanisms of lava extrusion (spine versus blocky dome). We additionally consider our data on the mechanical and hydraulic properties of dacites relevant for models of outgassing and assessments of the structural stability of dacitic volcanoes worldwide. Eruptive activity at MSH, an active stratovolcano belonging to the Cascade volcanic arc of North America (located in Skamania County in Washington (USA); Fig. 1a), has recently produced episodes of dome-growth (1980–1986) and spine-growth (2004–2008) and therefore represents an ideal natural laboratory to undertake such a study.

The eruptive history of MSH has been divided into nine distinct periods: Ape Canyon, Cougar, Swift Creek, Smith Creek, Pine Creek, Castle Creek, Sugar Bowl, Kalama, and Goat Rocks (Lipman and Mullineaux, 1981). These periods are characterised by episodes of dome-building, explosive eruptions, pyroclastic flows, and lahars. The erupted products

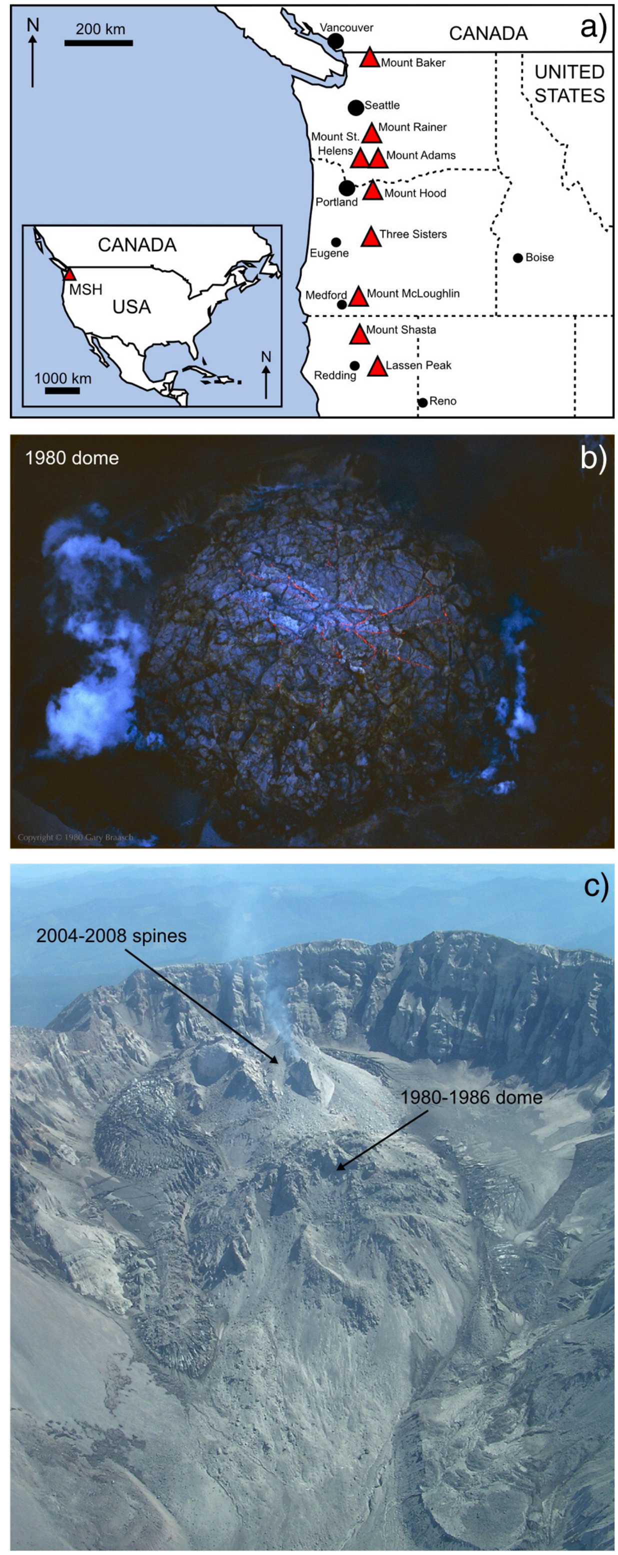

Fig. 1. Mount St. Helens (MSH). (a) Map showing the volcanoes of the Cascade Volcanic Arc of North America. Inset shows the location of MSH in North America. (b) Aerial view of the 1980 lava dome at MSH. Copyright © 1980 Gary Braasch Photography. Photograph used here with permission from Gary Braasch. (c) Aerial view of the crater at MSH (photograph taken September 2006; photo credit: Kelly Russell) showing the 1980–1986 domes and the spines of the 2004–2008 eruption.

are mainly dacite with subordinate andesite and basalt (e.g., Castle Creek eruptive period; Lipman and Mullineaux, 1981). MSH gained most of its attention and notoriety for the devastating eruption that

Please cite this article as: Heap, M.J., et al., Mechanical behaviour of dacite from Mount St. Helens (USA): A link between porosity and lava dome extrusion mechanism (dome or spi..., J. Volcanol. Geotherm. Res. (2016), http://dx.doi.org/10.1016/j.jvolgeores.2016.10.015

began on the 18th of May 1980. On that day, a magnitude 5.1 earthquake triggered the collapse of the northern flank of the volcano, initiating a Plinian eruption (Lipman and Mullineaux, 1981). The explosive Plinian phase of the eruption was followed by two main periods of effusive volcanism, expressed as a series of dacitic lava domes or lobes (1980–1986; Swanson and Holcomb, 1990; Rutherford and Hill, 1993; Blundy and Cashman, 2001; Fig. 1b and c) and spine or whaleback features (2004–2008; Iverson et al., 2006; Pallister et al., 2008; Cashman et al., 2008; Vallance et al., 2008; Kennedy et al., 2009; Smith et al., 2011; Kendrick et al., 2012; Pallister et al., 2013; Fig. 1c). Although the dacites of the 2004–2008 eruption are more silica-rich than the 1980–1986 dome rocks (~65 wt.% versus ~63 wt.%, respectively), their major and trace element compositions are broadly similar (Swanson and Holcomb, 1990; Pallister et al., 2008).

3. Experimental campaign

3.1. Previous relevant studies

Our knowledge of the mechanical behaviour of sedimentary rocks, such as sandstone, is comprehensive (Wong et al., 1997; Wong and Baud, 2012). Despite its importance, our knowledge and understanding of the mechanical behaviour of volcanic rocks is comparatively embryonic. Volcanic rocks offer a much more varied and complex microstructure than sedimentary rocks. For example, (1) volcanic rocks often contain a dual modes of porosity expressed as microcracks and primary pores (Heap et al., 2014a), (2) the abundance (Kueppers et al., 2005), mean diameter, and diameter size distribution (Shea et al., 2010) of the pores can vary significantly, (3) the density and length of microcracks can vary significantly (Heap et al., 2014a; Kushnir et al., 2016), (4) volcanic rocks have variable crystallinity that can vary in shape, mean size, and size distribution (Marsh, 1988; Armienti, 2008), (5) the groundmass of a volcanic rock can be variably crystallised (Geschwind and Rutherford, 1995; Blundy and Cashman, 2001) and, (6) volcanic rocks can be variably altered (Pola et al., 2012; Ball et al., 2013; Horwell et al., 2013; Wyering et al., 2014).

Recently, studies have begun to explore the mechanical behaviour and failure modes of volcanic rocks. Triaxial deformation experiments have been performed on andesite (Bauer et al., 1981; Smith et al., 2009; Loaiza et al., 2012; Heap et al., 2015a, 2015b; Farquharson et al., 2016a; Heap and Wadsworth, 2016; Siratovich et al., 2016), tuff (Zhu et al., 2011; Heap et al., 2015b), basalt (Bauer et al., 1981; Shimada, 1986; Violay et al., 2012; Adelinet et al., 2013; Violay et al., 2015; Zhu et al., 2016; reviewed in Heap et al., 2017), and dacite (Kennedy et al., 2009; Smith et al., 2011; Kennedy and Russell, 2012). These studies have highlighted that, while the failure mode of low-porosity volcanic rock remains staunchly brittle, the failure mode of high-porosity volcanic rock can switch from brittle to ductile at elevated pressure (depth). While the deformation of volcanic rocks in the brittle field is manifest as localised axial splits or shear fractures, the ductile regime is characterised by either distributed cataclastic pore collapse (Zhu et al., 2011; Heap et al., 2015b) or the formation of localised bands of compacted pores (Loaiza et al., 2012; Adelinet et al., 2013; Heap et al., 2015a).

The recent studies probing the mechanical behaviour and failure mode of volcanic rocks, listed above, are biased towards basalts and andesites. Relatively few triaxial deformation experiments have been performed on dacite (Kennedy et al., 2009; Smith et al., 2011; Kennedy and Russell, 2012). Differences in magma composition dictate differences in thermodynamic and transport properties (e.g., Lesher and Spera, 2015) and solidification resulting in rocks with very different physical and textural properties (e.g., pore size and shape). This virtually guarantees significant differences in the mechanical and hydraulic behaviour of volcanic rocks as a function of composition (basalt versus andesite versus dacite). Kennedy et al. (2009) performed room temperature experiments on dacite from the 2004–2008 spines of MSH (porosity = 0.07–0.08; the results of more experiments on these materials are available in Kennedy and Russell, 2012) and Augustine volcano (USA) (porosity = 0.2–0.24). They show that the low-porosity dacite from MSH remained brittle up to a confining pressure of 75 MPa (depth ~3 km). The high-porosity Augustine dacite was ductile at pressures from 25 to 75 MPa (depth ~1–3 km). Smith et al. (2011) deformed dacites from the 2004–2008 spines of MSH (porosity = 0.08–0.197) under a range of confining pressures (up to 10 MPa), temperatures (up to 970 °C), and strain rates (from 10^{-4} to 10^{-6} s^{-1}). They found that, despite the different experimental conditions, the failure mode remained brittle (with the exception of one experiment performed at 10 MPa and 850 °C). The brittle failure mode of dacite from MSH at high temperature is attributed to the highly crystallised nature of the extruded materials (Smith et al., 2011).

3.2. Experimental materials

Cylindrical core samples (20 mm in diameter and precision-ground to a nominal length of 40 mm) were prepared from two blocks (MSH1 and MSH2; approximately 20 × 20 × 20 cm) collected from the 1980 dome at MSH. The natural material extruded during an eruption will exhibit some variation and, thus, we chose two blocks from 1980 dome lava that best capture the natural heterogeneity. Sample photographs and backscattered scanning electron microscope (SEM) photographs of both rocks are presented in Fig. 2. MSH1 contains abundant microcracked plagioclase (long axis ~500–1000 μm) and subordinate pyroxene and amphibole phenocrysts (long axis ~200 μm) held within a wispy glassy groundmass containing an abundance of higher-density Fe-Ti oxides (magnetite and ilmenite; Rutherford and Hill, 1993) (Fig.

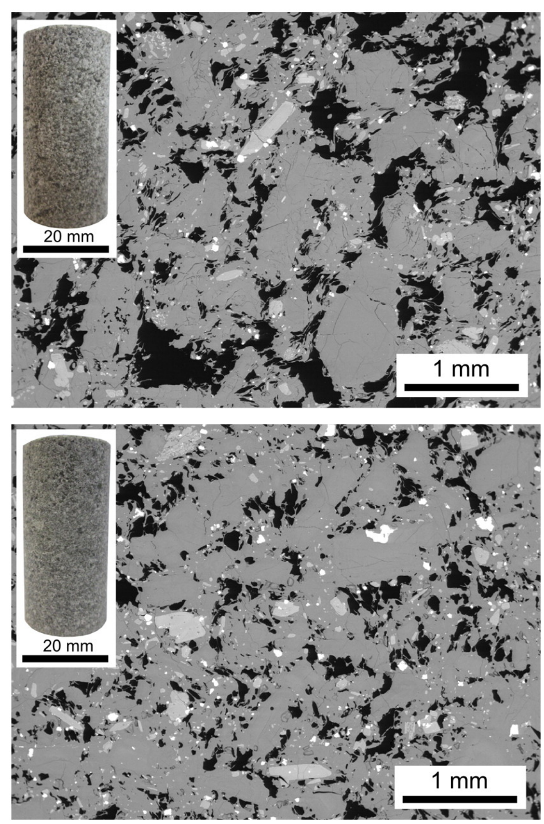

Fig. 2. Microstructure. (a) Backscattered scanning electron (SEM) image of the as-collected (intact) MSH 1980 dome lava MSH1. (b) SEM image of the as-collected (intact) MSH 1980 dome lava MSH2. Greyscale corresponds to density on both images: light colours are high-density, and vice versa. Porosity is black. High-density Fe-Ti oxides (magnetite and ilmenite) can be seen as small, white crystals. Photographs of cylindrical samples of MSH1 and MSH2 used for the laboratory testing are provided as insets on the relevant image.

Table 1
Summary of the porosity-permeability data unique to this study, and those from Klug and Cashman (1996) and Gaunt et al. (2014, 2016). The 5 MPa confining pressure quoted for the Gaunt et al. (2014, 2016) data is an effective pressure (confining pressure = 10 MPa; average pore pressure = 5 MPa) (labelled with asterisks). Table shows room temperature data only (high-temperature data from Gaunt et al. (2016) are excluded). v = vertical; h = horizontal; K and C (1996) = Klug and Cashman (1996).

Reference	Location	Sample	Connected porosity	Confining pressure (MPa)	Pore fluid	Permeability (m^2)
This study	1980 dome	MSH1 01	0.322	1	Nitrogen	3.03×10^{-12}
This study	1980 dome	MSH1 02	0.321	1	Nitrogen	2.84×10^{-12}
This study	1980 dome	MSH1 03	0.291	1	Nitrogen	4.36×10^{-13}
This study	1980 dome	MSH1 04	0.303	1	Nitrogen	5.42×10^{-13}
This study	1980 dome	MSH1 05	0.318	1	Nitrogen	1.64×10^{-12}
This study	1980 dome	MSH1 06	0.333	1	Nitrogen	2.26×10^{-12}
This study	1980 dome	MSH1 07	0.307	1	Nitrogen	4.68×10^{-13}
This study	1980 dome	MSH1 08	0.367	1	Nitrogen	2.82×10^{-12}
This study	1980 dome	MSH1 09	0.312	1	Nitrogen	1.42×10^{-12}
This study	1980 dome	MSH2 01	0.196	1	Nitrogen	7.24×10^{-15}
This study	1980 dome	MSH2 02	0.184	1	Nitrogen	1.91×10^{-15}
This study	1980 dome	MSH2 03	0.223	1	Nitrogen	1.45×10^{-14}
This study	1980 dome	MSH2 04	0.199	1	Nitrogen	5.29×10^{-15}
This study	1980 dome	MSH2 05	0.183	1	Nitrogen	1.08×10^{-15}
This study	1980 dome	MSH2 06	0.179	1	Nitrogen	1.24×10^{-15}
This study	1980 dome	MSH2 07	0.191	1	Nitrogen	2.16×10^{-15}
This study	1980 dome	MSH2 08	0.197	1	Nitrogen	7.57×10^{-15}
K and C (1996)	May 18, 1980 eruption	Blast dacite	0.308	0	Nitrogen	3.21×10^{-14}
K and C (1996)	May 18, 1980 eruption	Blast dacite	0.321	0	Nitrogen	6.29×10^{-14}
K and C (1996)	May 18, 1980 eruption	Blast dacite	0.318	0	Nitrogen	1.12×10^{-13}
K and C (1996)	May 18, 1980 eruption	Blast dacite	0.347	0	Nitrogen	5.82×10^{-14}
K and C (1996)	May 18, 1980 eruption	Blast dacite	0.370	0	Nitrogen	2.27×10^{-13}
K and C (1996)	May 18, 1980 eruption	Blast dacite	0.329	0	Nitrogen	1.38×10^{-12}
K and C (1996)	May 18, 1980 eruption	Blast dacite	0.387	0	Nitrogen	4.06×10^{-14}
K and C (1996)	May 18, 1980 eruption	Blast dacite	0.401	0	Nitrogen	8.34×10^{-14}
K and C (1996)	May 18, 1980 eruption	Blast dacite	0.414	0	Nitrogen	1.07×10^{-13}
K and C (1996)	May 18, 1980 eruption	Blast dacite	0.429	0	Nitrogen	1.75×10^{-13}
K and C (1996)	May 18, 1980 eruption	Blast dacite	0.456	0	Nitrogen	1.90×10^{-13}
K and C (1996)	May 18, 1980 eruption	Blast dacite	0.450	0	Nitrogen	1.37×10^{-13}
K and C (1996)	May 18, 1980 eruption	Blast dacite	0.424	0	Nitrogen	6.66×10^{-14}
K and C (1996)	May 18, 1980 eruption	Blast dacite	0.433	0	Nitrogen	4.21×10^{-14}
K and C (1996)	May 18, 1980 eruption	Blast dacite	0.401	0	Nitrogen	2.42×10^{-14}
K and C (1996)	May 18, 1980 eruption	Blast dacite	0.398	0	Nitrogen	1.46×10^{-14}
K and C (1996)	May 18, 1980 eruption	Blast dacite	0.431	0	Nitrogen	2.61×10^{-14}
K and C (1996)	May 18, 1980 eruption	Blast dacite	0.457	0	Nitrogen	1.48×10^{-14}
K and C (1996)	May 18, 1980 eruption	Blast dacite	0.475	0	Nitrogen	5.76×10^{-14}
K and C (1996)	May 18, 1980 eruption	Blast dacite	0.487	0	Nitrogen	7.35×10^{-14}
K and C (1996)	May 18, 1980 eruption	Blast dacite	0.481	0	Nitrogen	1.77×10^{-13}
K and C (1996)	May 18, 1980 eruption	Blast dacite	0.496	0	Nitrogen	2.33×10^{-13}
K and C (1996)	May 18, 1980 eruption	Blast dacite	0.527	0	Nitrogen	1.53×10^{-13}
K and C (1996)	May 18, 1980 eruption	Plinian pumice	0.752	0	Nitrogen	5.63×10^{-13}
K and C (1996)	May 18, 1980 eruption	Plinian pumice	0.761	0	Nitrogen	1.57×10^{-12}
Gaunt et al. (2014)	2004–2008 spine	Fault gouge (v)	0.286	5*	Distilled water	1.59×10^{-14}
Gaunt et al. (2014)	2004–2008 spine	Fault gouge (h)	0.286	5*	Distilled water	3.80×10^{-18}
Gaunt et al. (2014)	2004–2008 spine	Cataclastic breccia (v)	0.119	5*	Distilled water	1.82×10^{-14}
Gaunt et al. (2014)	2004–2008 spine	Cataclastic breccia (h)	0.119	5*	Distilled water	3.81×10^{-16}
Gaunt et al. (2014)	2004–2008 spine	Sheared dacite (v)	0.100	5*	Distilled water	2.96×10^{-16}
Gaunt et al. (2014)	2004–2008 spine	Sheared dacite (h)	0.100	5*	Distilled water	4.50×10^{-16}
Gaunt et al. (2014)	2004–2008 spine	Massive dacite (v)	0.056	5*	Distilled water	2.85×10^{-16}
Gaunt et al. (2014)	2004–2008 spine	Massive dacite (h)	0.056	5*	Distilled water	3.50×10^{-16}
Gaunt et al. (2016)	2004–2008 spine	Massive dacite	0.06	5*	Distilled water	5.46×10^{-16}
Gaunt et al. (2016)	2004–2008 spine	Massive dacite	0.06	5*	Distilled water	5.76×10^{-16}

2a). The long axis of the pores is typically between 50 and 500 μm and are deformed to irregular, elongate shapes; some pore walls are only a couple of μm thick (Fig. 2a). Sample MSH2 also contains microcracked plagioclase phenocrysts (long axis ~500–1000 μm) and phenocrysts of pyroxene and amphibole (long axis ~200 μm) held within an oxide-bearing glassy groundmass (Fig. 2b). MSH2 is denser than MSH1 (porosity appears as black on the SEM images). The long axis of the pores, which are generally less deformed than those in MSH1, is ~50 μm (Fig. 2b). Although our samples were collected from the 1980 dome, we highlight that the phenocryst assemblage did not change during the 1980–1986 activity (Rutherford and Hill, 1993). Further, the magma discharge rate did not drastically alter: 1.8×10^6 m^3/month (1980–1981), 1.3×10^6 m^3/month (1982–1984), and 0.62×10^6 m^3/month (1984–1986) (Swanson and Holcomb, 1990). As a result, the 1980 dome samples collected for this study could be considered analogous to the dacites extruded during the entire eruptive sequence.

3.3. Physical property measurement protocol

The connected porosity of each core was determined using a helium pycnometer. Their permeabilities were then measured using a benchtop steady-state gas (nitrogen) permeameter at the Institut de Physique du Globe de Strasbourg (IPGS) (Heap and Kennedy, 2016; Farquharson et al., 2016b). All permeability measurements were conducted under a confining pressure of 1 MPa. Volumetric flow rate Q measurements were taken (using a gas flowmeter) under several pressure gradients ΔP (defined here as the upstream pressure P_u minus the downstream pressure P_d). P_d is simply the atmospheric pressure (taken here to be

Please cite this article as: Heap, M.J., et al., Mechanical behaviour of dacite from Mount St. Helens (USA): A link between porosity and lava dome extrusion mechanism (dome or spi..., J. Volcanol. Geotherm. Res. (2016), http://dx.doi.org/10.1016/j.jvolgeores.2016.10.015

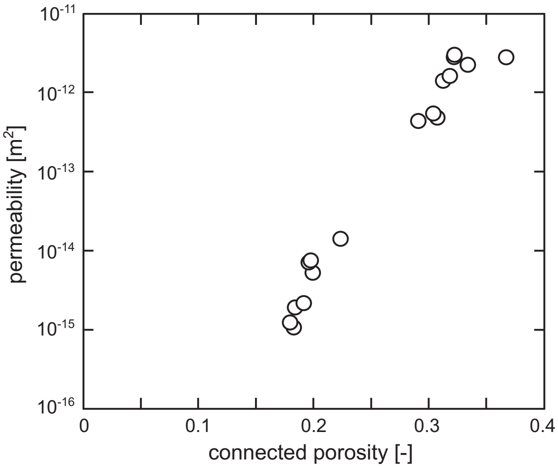

Fig. 3. Permeability as a function of connected porosity for the 1980 MSH dome samples collected for this study plotted using log-linear axes (data available in Table 1).

101,325 Pa). Values of ΔP were typically from 0.05 to 0.2 MPa, equating to flow rates between 5 and 500 ml.min^{-1}. The slope of the graph of Q as a function of ΔP multiplied by the mean pore fluid pressure P_m (i.e., $(P_u + P_d)/2$) yields the raw permeability k_{raw} using the following relation:

$$k_{raw} = \frac{dQ}{d(\Delta P \cdot P_m)} \frac{(\mu L P_d)}{A}, \quad (1)$$

where μ is the viscosity of the pore fluid (taken as the viscosity of nitrogen at 20 °C = 1.76×10^{-5} Pa.s), and L and A are the sample length and cross sectional area, respectively. We first plot $1/k_{raw}$ as a function of Q to check whether the Forchheimer correction is required. The correction—required for each of the experiments performed here—is necessary if the data can be well described by a positive linear slope. The Forchheimer-corrected permeability k_{forch} is the inverse of the y-intercept of the best-fit linear regression in the plot of $1/k_{raw}$ as a function of Q. To check whether the Klinkenberg correction is also required (i.e., that both corrections are needed), we plot k_{forch} as a function of $1/P_m$. The Klinkenberg correction is required if the data can be well described by a positive linear slope, which was not the case for any of our experiments. For all experiments k_{forch} was therefore taken as the true permeability.

3.4. Uniaxial and triaxial experiment protocol

The cylindrical samples were vacuum-saturated with distilled water prior to their deformation. The samples were deformed either uniaxially or triaxially. Uniaxial compressive strength (UCS) measurements were

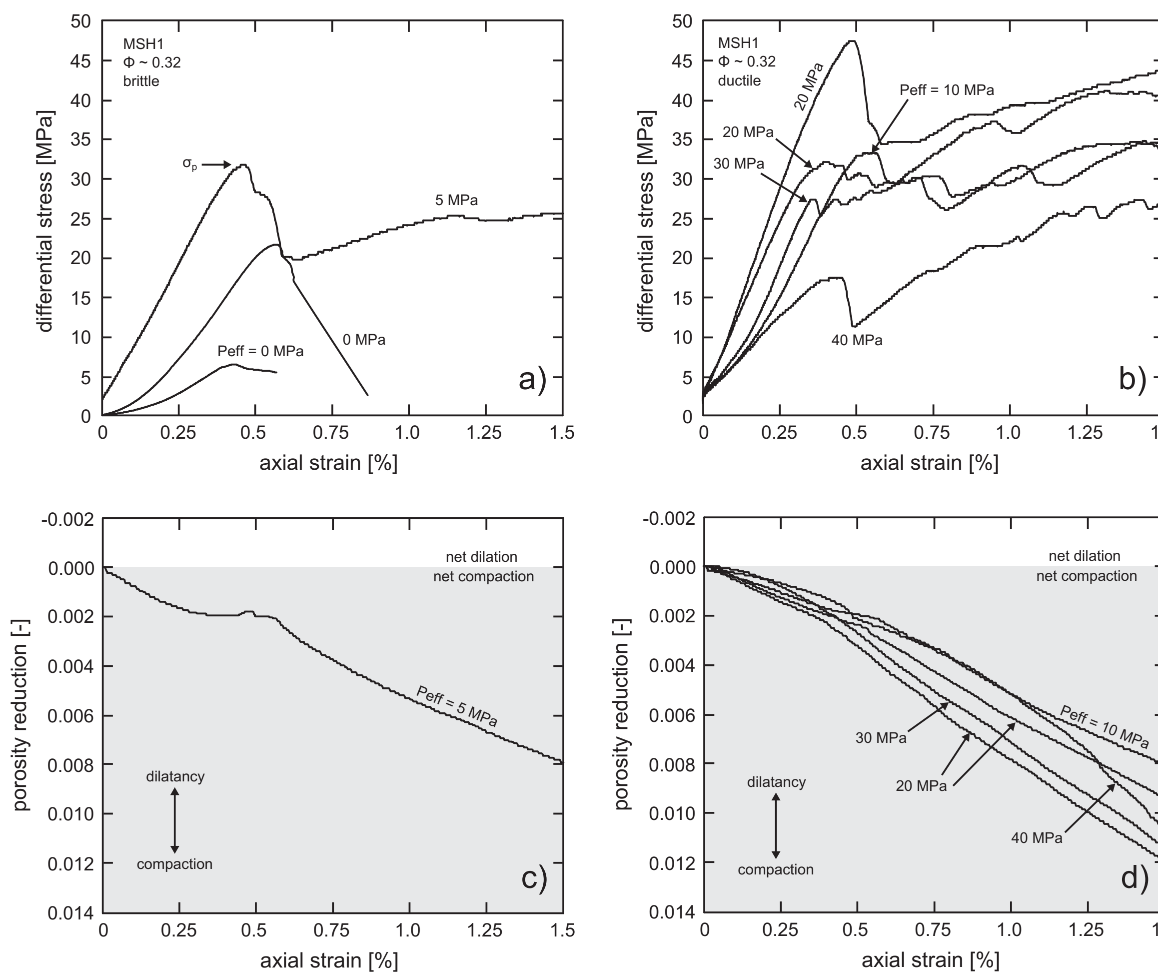

Fig. 4. Brittle (a) and ductile (b) stress-strain curves for samples of MSH1 (porosity ~0.3) deformed at a constant strain rate. The effective pressure (Peff) is indicated next to each curve. The position of the peak stress is a brittle experiment σ_p is labelled for the experiment at *Peff* = 5 MPa (panel (a)). (c) The porosity reduction curve for the sample deformed at *Peff* = 5 MPa from panel (a). Grey zone denotes zone of net porosity decrease. (d) The porosity reduction curves for the experiments shown in panel (b). Grey zone denotes zone of net porosity decrease.

Please cite this article as: Heap, M.J., et al., Mechanical behaviour of dacite from Mount St. Helens (USA): A link between porosity and lava dome extrusion mechanism (dome or spi..., J. Volcanol. Geotherm. Res. (2016), http://dx.doi.org/10.1016/j.jvolgeores.2016.10.015

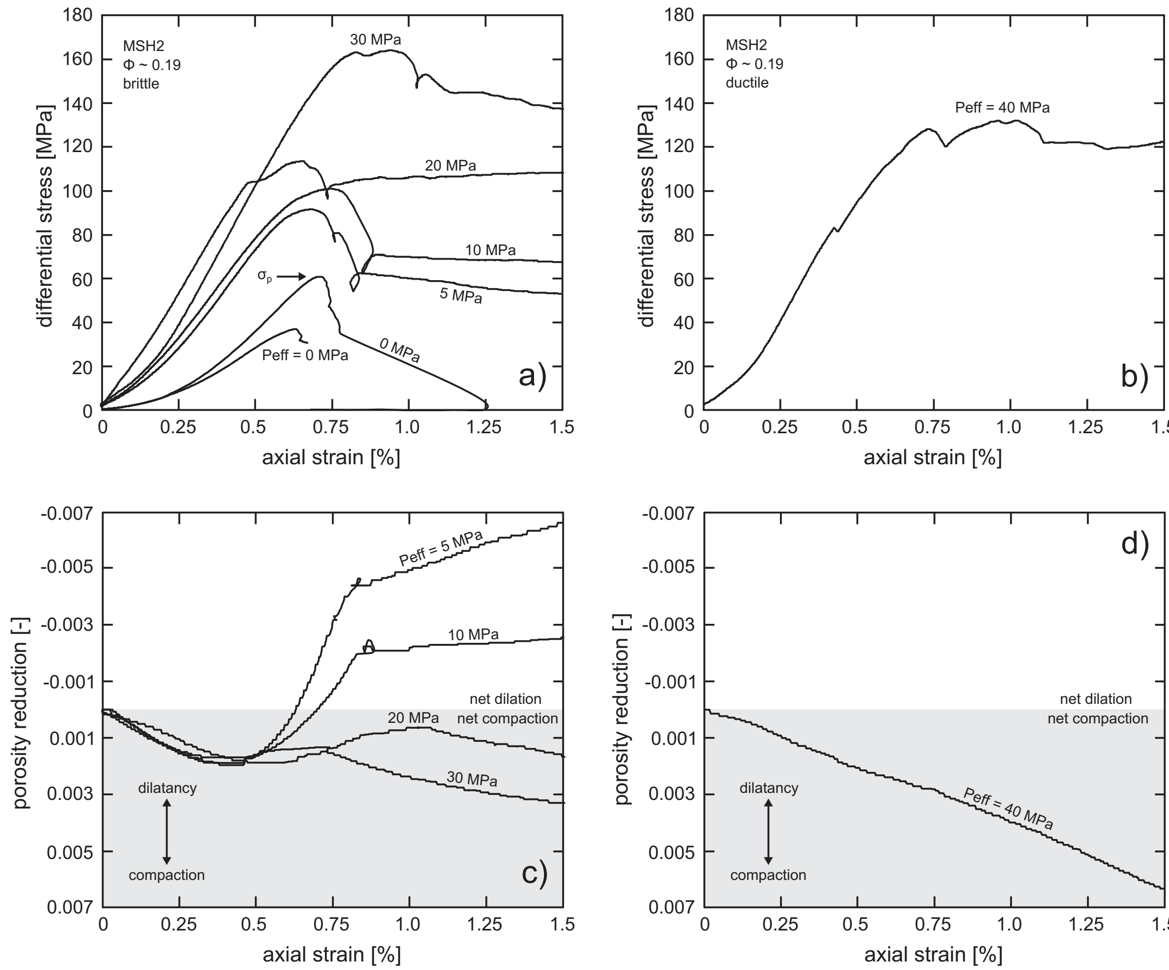

Fig. 5. Brittle (a) and ductile (b) stress-strain curves for samples of MSH2 (porosity ~0.19) deformed at a constant strain rate. The effective pressure (*Peff*) is indicated next to each curve. σ_p, labelled for the experiment at *Peff* = 0 MPa (panel (b)), marks the position of the peak stress in a brittle experiment. (c) The porosity reduction curves for the samples deformed at *Peff* = 5, 10, 20, and 30 MPa from panel (a). Grey zone denotes zone of net porosity decrease. (d) The porosity reduction curve for the sample deformed at *Peff* = 40 MPa from panel (b). Grey zone denotes zone of net porosity decrease.

conducted on water-saturated samples in a uniaxial load frame (Schenk) at IPGS. Samples were deformed inside a water bath at a constant strain rate of 1×10^{-5} s^{-1} until macroscopic failure (formation of a throughgoing fracture). During experimentation, axial force was measured by a load cell and axial displacement by a linear variable differential transducer (LDVT) that measured the displacement of the piston relative to the static base plate. These measurements were converted to uniaxial stress and strain using the sample dimensions.

Triaxial experiments were performed on jacketed (nitrile) water-saturated samples using a triaxial deformation apparatus at IPGS. All triaxial deformation experiments were performed in compression. Experiments were performed at a constant pore fluid pressure *Pp* (distilled water) of 10 MPa and at confining pressures *Pc* (kerosene) between 15 and 50 MPa provided by servo-controlled pore and confining pressure intensifiers, respectively. These conditions equate to effective pressures *Peff* between 5 and 40 MPa (equating to depths between near-surface and 1.5–2 km). We assume here a simple effective pressure law $Peff = Pc - \alpha Pp$ where poroelastic constant α is equal to one; a recent study by Farquharson et al. (2016a) found that α is extremely close to unity for an andesite containing a porosity of 0.09, validating our assumption. Samples were deformed at a constant strain rate of 1×10^{-5} s^{-1} until an axial strain of 1.5% was reached. Measurements of axial force and displacement, converted to axial stress and strain using the sample dimensions, were measured using a load cell and an LVDT that measured the displacement of the piston. Pore volume change during deformation was measured by an LVDT monitoring the position of the piston inside the pore pressure intensifier; this volume was converted to a porosity change using the sample dimensions. Sample drainage at the chosen strain rate is expected due to the relatively high permeability of our test samples (Table 1) (Heap and Wadsworth, 2016). An acoustic emission (AE) transducer attached to the top of the piston recorded the output of AE energy (the root-mean-square of the received waveform) during deformation. AE's are high frequency elastic wave packets generated by the rapid release of strain energy, interpreted here as the result of microcracking within the sample (e.g., Lockner, 1993).

We also performed a hydrostatic ($\sigma_1 = \sigma_2 = \sigma_3$) experiment on a sample of MSH1. During a hydrostatic test, the confining pressure is increased on a sample whilst maintaining a constant pore fluid pressure ($Pp = 10$ MPa). The purpose of such an experiment is to measure porosity loss during hydrostatic loading and, ultimately, to find the onset pressure of inelastic hydrostatic compaction due to cataclastic pore collapse, termed P^* (Wong and Baud, 2012). Pore volume change in our hydrostatic experiment—measured by the pore pressure intensifier—was converted to porosity change using the sample dimensions.

4. Results

4.1. Porosity-permeability relationship

Permeability as a function of porosity is presented as Fig. 3 and in Table 1. The permeability of the samples, which vary in porosity from 0.184 to 0.367, ranges from 10.8×10^{-15} to 3.03×10^{-12} m^2. Our

Please cite this article as: Heap, M.J., et al., Mechanical behaviour of dacite from Mount St. Helens (USA): A link between porosity and lava dome extrusion mechanism (dome or spi..., J. Volcanol. Geotherm. Res. (2016), http://dx.doi.org/10.1016/j.jvolgeores.2016.10.015

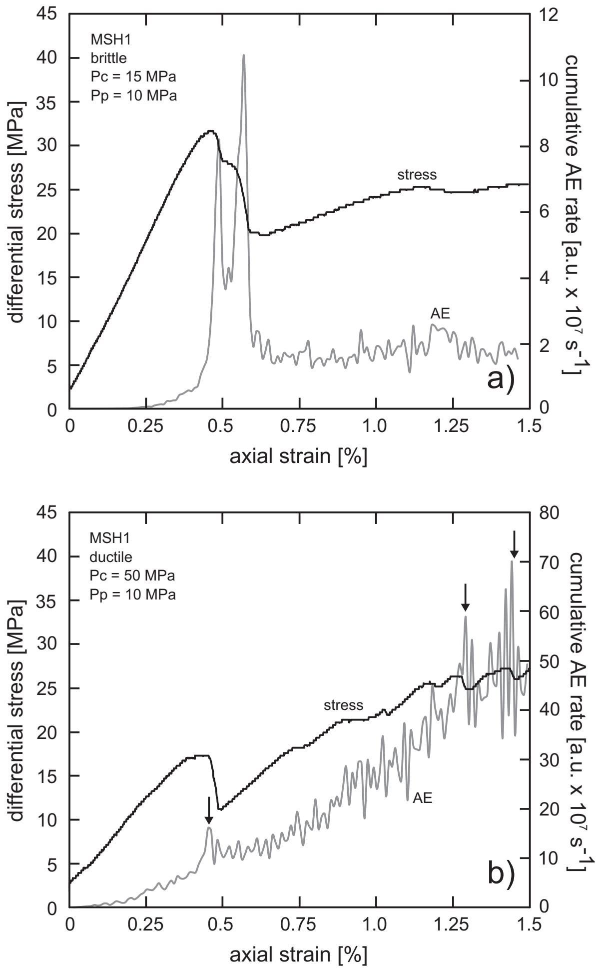

Fig. 6. Stress-strain curves for the samples deformed at *Peff* = 5 MPa from Fig. 4a (a) and at *Peff* = 40 MPa from Fig. 4b (b) plotted with the output of acoustic emission energy released during deformation. Arrows on panel (b) highlight spikes in acoustic emission activity that are contemporaneous with stress drops in the mechanical data.

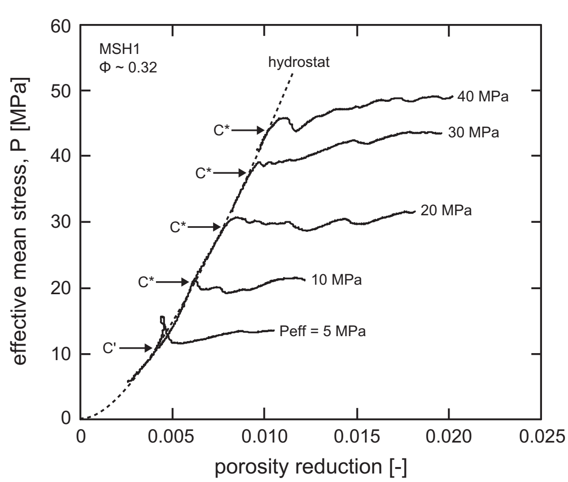

Fig. 7. Effective mean stress (P)-porosity reduction curves for MSH1 (porosity ~0.3). The effective pressure (*Peff*) is indicated next to each curve. The positions of the onset of dilatational microcracking (C') and the onset of inelastic pore collapse (C^*) are indicated for each experimental curve.

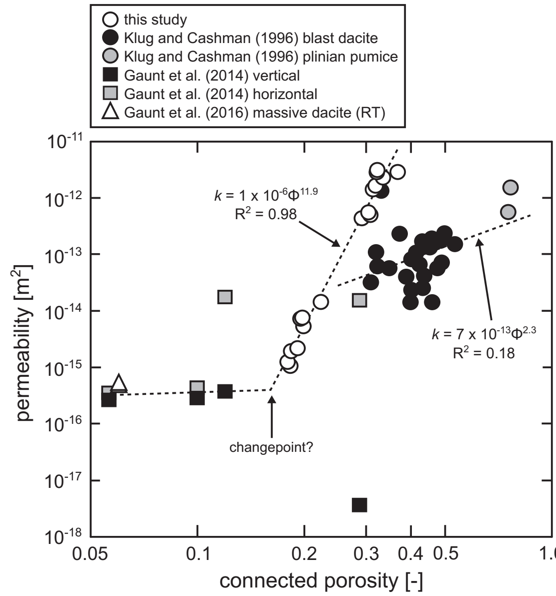

Fig. 8. Permeability as a function of connected porosity for the 1980 dome samples collected for this study and room-temperature data taken from Klug and Cashman (1996) and Gaunt et al. (2014, 2016) plotted using log-log axes (all data available in Table 1). Power law trends for the data of this study and the data of Klug and Cashman (1996), and their coefficients of determination, are provided on the figure.

data also show that permeability increases as porosity is increased (Fig. 3; Table 1).

4.2. Mechanical data

Our experiments were first assigned a failure mode. The failure mode of rock is often classified as either brittle or ductile (Rutter, 1986; Evans et al., 1990; Paterson and Wong, 2005; Wong and Baud, 2012). We use these definitions here to describe deformation on the sample lengthscale. A brittle experiment typically involves an increase in porosity as macroscopic failure is approached—the result of dilatational microcracking—and strain softening (i.e., a stress drop) following a peak stress. The formation of axial splits and shear fractures within the post-deformation experimental sample—i.e. strain localisation—is the hallmark of brittle deformation. We adopt here the definition of ductility of Rutter (1986): the capacity of a material to deform to a substantial strain without the tendency to localise the flow into faults (although there are instances of compaction localisation in the ductile domain, see Baud et al., 2004). Ductility, according to Rutter (1986) and the authors of this study, is not dependent on the mechanism of deformation. Therefore, and although similar stress-strain curves may be generated, ductility can occur by very different micromechanisms, including viscous flow (e.g., Cordonnier et al., 2012), crystal-plastic flow (e.g., Rutter et al., 1994), and cataclastic flow (distributed microcracking; e.g., Menéndez et al., 1996). Ductile experiments are typically purely compactant (Wong and Baud, 2012). Ductile flow in rocks under a constant strain rate can proceed at a roughly constant stress or exhibit strain hardening (Wong and Baud, 2012). Instances of compaction localisation (compaction bands or bands of collapsed pores) are usually associated with small stress drops and bursts in AE activity (Baud et al., 2004). A ductile failure mode is confirmed by the absence of axial splits and shear fractures within the post-deformation experimental sample.

Given the tenets described above, the experiments performed on MSH1 (porosity ~0.32) at an effective pressure of 0 (i.e., uniaxial) and 5 MPa were brittle (Fig. 4a and c). The experiments performed on MSH2 (porosity ~0.19) were brittle at effective pressures between 0 and 30 MPa (Fig. 5a and c). In the brittle regime, the stress first increases non-linearly as a function of increasing strain (Figs. 4a and 5a). This is often attributed to the closure of pre-existing microcracks orientated perpendicular or sub-perpendicular to the direction of the maximum principal stress (as evidenced by the decrease in sample porosity during this stage; Figs. 4c and 5c). The microcrack closure stage is followed by quasi-linear elastic behaviour (Figs. 4a and 5a). Departure from elasticity is signalled by the stress decreasing non-linearly as a function of increasing strain (Figs. 4a and 5a), the result of the nucleation and growth of microcracks. The onset of inelastic (permanent) deformation, termed C' (Wong et al., 1997), is also signalled by the onset of AE activity (Fig. 6a). The formation and growth of microcracks slows the rate of sample compaction until the porosity of the sample starts to increase (Figs. 4c and 5c). Strain-softening behaviour follows a peak stress (σ_p; Figs. 4a and 5a), during which the macroscopic shear fracture forms. Sliding on the resultant shear fracture at the residual frictional strength accommodates any additional post-failure strain (Figs. 4a and 5a). Sliding on the shear fracture results in a porosity decrease (Figs. 4c and 5c), the product of the comminution and compaction of particles within the shear band.

The experiments performed on MSH1 (porosity ~0.32) at an effective pressure of 10, 20, 30, and 40 MPa were ductile (Fig. 4b and d), while MSH2 (porosity ~0.19) was ductile at an effective pressure of only 40 MPa (Fig. 5b and d). The ductile curves also contain the above-described microcrack closure and quasi-linear elastic phases of deformation (Figs. 4b and 5b). The onset of inelastic compaction in ductile experiments is termed C^* (Wong et al., 1997), and is identified as an inflection point in the porosity change curve (Figs. 4d and 5d) or the onset of an acceleration of AE activity (Fig. 6b). We note that all of the curves display strain hardening (Figs. 4b and 5b) and are compactant throughout (Figs. 4d and 5d). We further highlight the presence of stress drops during the compaction of MSH1 (Fig. 4b) and MSH2 (Fig. 5b) and that these stress drops are accompanied by increases in the output of AE energy (Fig. 6b).

It is common in rock deformation studies to plot the effective mean stress (P), where $P = ((\sigma_1 + 2\,\sigma_3) - Pp$, as a function of porosity change, as shown in Fig. 7 for the MSH1 experiments of this study (sample MSH1_3 is excluded due to its high strength arising from its anomalously low porosity). Curves of this type are used to better observe the role of shear stress on the evolution of porosity. The first deviation of the experimental curves from the hydrostatic ($\sigma_1 = \sigma_2 = \sigma_3$; see Section 3.4 for the experimental protocol for a hydrostatic experiment) curve indicates the onset of inelastic behaviour in each experiment (i.e., the position of C' in the brittle regime and C^* in the ductile regime, as indicated in Fig. 7).

5. Discussion

5.1. Porosity-permeability relationships for dacite

The porosity-permeability data of this study are plotted alongside previously-published room-temperature data from Klug and Cashman (1996) and Gaunt et al. (2014, 2016) in Fig. 8 (see Table 1). We find that the porosity-permeability data for the 1980 lava dome samples—the data of this study—are well-described by a single power law (Fig. 8). This is in contrast to recent studies on the permeability of volcanic rocks (andesites, basaltic-andesites, and dacites) that invoke a two-power law model (Heap et al., 2014a, 2015c; Farquharson et al., 2015; Kushnir et al., 2016; Heap and Kennedy, 2016). The switch from one power law to the next is thought to represent a microstructural change in void space connectivity. The pore network does not form a permeable backbone in the low-porosity volcanic rocks that are described by the first power law (which has a high exponent), forcing fluids to travel through narrow, tortuous microcracks that connect neighbouring pores. The change to a power law with a lower exponent—dubbed the “changepoint porosity”—marks the threshold porosity for which the pore network is better connected; fluids in these samples rarely rely on tortuous microcracks to pass through the sample (Heap et al., 2014a, 2015c; Farquharson et al., 2015; Kushnir et al., 2016; Heap and Kennedy, 2016). The changepoint porosity in these studies was determined to occur at a value of porosity between 0.105 and 0.155, i.e. lower than the lowest porosity sample in our dataset (porosity = 0.179; Table 1). Therefore, all of our samples likely have a well-connected pore network (Fig. 2). It is possible therefore that a changepoint porosity may be encountered in rocks that preserve a lower porosity than those measured in this study. If we include the data of Gaunt et al. (2014, 2016) in our analysis, a changepoint exists at a porosity of ~0.15 (excluding those datapoints with permeabilities of ~10^{-14} and ~10^{-18} m^2; Fig. 8). In accordance with previous interpretations of the changepoint porosity (Heap et al., 2014a, 2015c; Farquharson et al., 2015; Kushnir et al., 2016; Heap and Kennedy, 2016), the low-porosity dacite samples from Gaunt et al. (2014, 2016) contain few pores and a pervasive microcrack network, while the rocks of this study contain a presumably well connected pore network (Fig. 2). However, a firm conclusion as to the existence of a changepoint porosity requires more data, especially at low to intermediate porosities.

Although the pumice data of Klug and Cashman (1996) do not necessarily allow for a power law relationship, the data cluster defines a trend with a substantially lower power law exponent (Fig. 8). Fluid flow in these pumices is facilitated by the pore network provided by their high porosities (Klug and Cashman, 1996). It is interesting to note that, despite their higher porosities, these pumice samples have much lower permeabilities than MSH1 (1980 dome rock; porosity ~0.32). Kushnir et al. (2016) also observed that basaltic-andesite dome rock was more permeable than higher-porosity pumice samples from Merapi (Indonesia). The reason likely lies in their different microstructures, a result of their different genesis. The high-porosity preserved in pumice often forms an extremely tortuous flow path (e.g., Wright et al., 2009; Kennedy et al., 2015); high-porosity dome rocks, on the other hand, can contain extremely well connected, and much more direct, flow paths (e.g., Farquharson et al., 2015; Kushnir et al., 2016).

Gaunt et al. (2014) provide permeability measurements for samples of dacitic lava dome material taken from a shear zone on the margin of one of the 2004–2008 spines. These data highlight how shearing can modify permeability and create a permeability anisotropy. As the spine margin is approached (i.e., the zone of foliated fault rocks), the rocks are increasingly permeable in the vertical direction, parallel to the foliation in the fault gouge, and become less permeable in the horizontal direction, perpendicular to the foliated fault rocks (Gaunt et al., 2014). Hence, the permeability anisotropy channels outgassed volatiles up through a fractured halo-zone surrounding the conduit (Gaunt et al., 2014); outgassing along the conduit margin is commonly observed at active stratovolcanoes (Rust et al., 2004; Lavallée et al., 2013; Farquharson et al., 2016a). Gaunt et al. (2016) offer permeability measurements for low-porosity dacite (from 28 January 2005) at high-temperature (we only plot room temperature data on Fig. 8). They show that permeability decreases with increasing temperature, inferred to be the consequence of the closure of pre-existing microcracks at high-temperature due to the thermal expansion of the mineral constituents. We speculate therefore that elevated temperatures will decrease the

Fig. 9. Post-deformation microstructure. (a) Backscattered scanning electron microscope (SEM) image of a sample of MSH1 deformed at $Peff = 5$ MPa (i.e., in the brittle regime). The form of the shear band is captured in the schematic inset. (b-c) SEM images of a sample of MSH1 deformed at $Peff = 40$ MPa (i.e., in the ductile regime). These images are higher magnification images of the band of collapsed pores from the areas indicated in panel (e). Arrows denote areas of discernible pore collapse. (d) The same SEM image as in panel (e), but with the band of collapsed pores highlighted. (e) Low-magnification image of the sample of MSH1 deformed at $Peff = 40$ MPa (i.e., in the ductile regime).

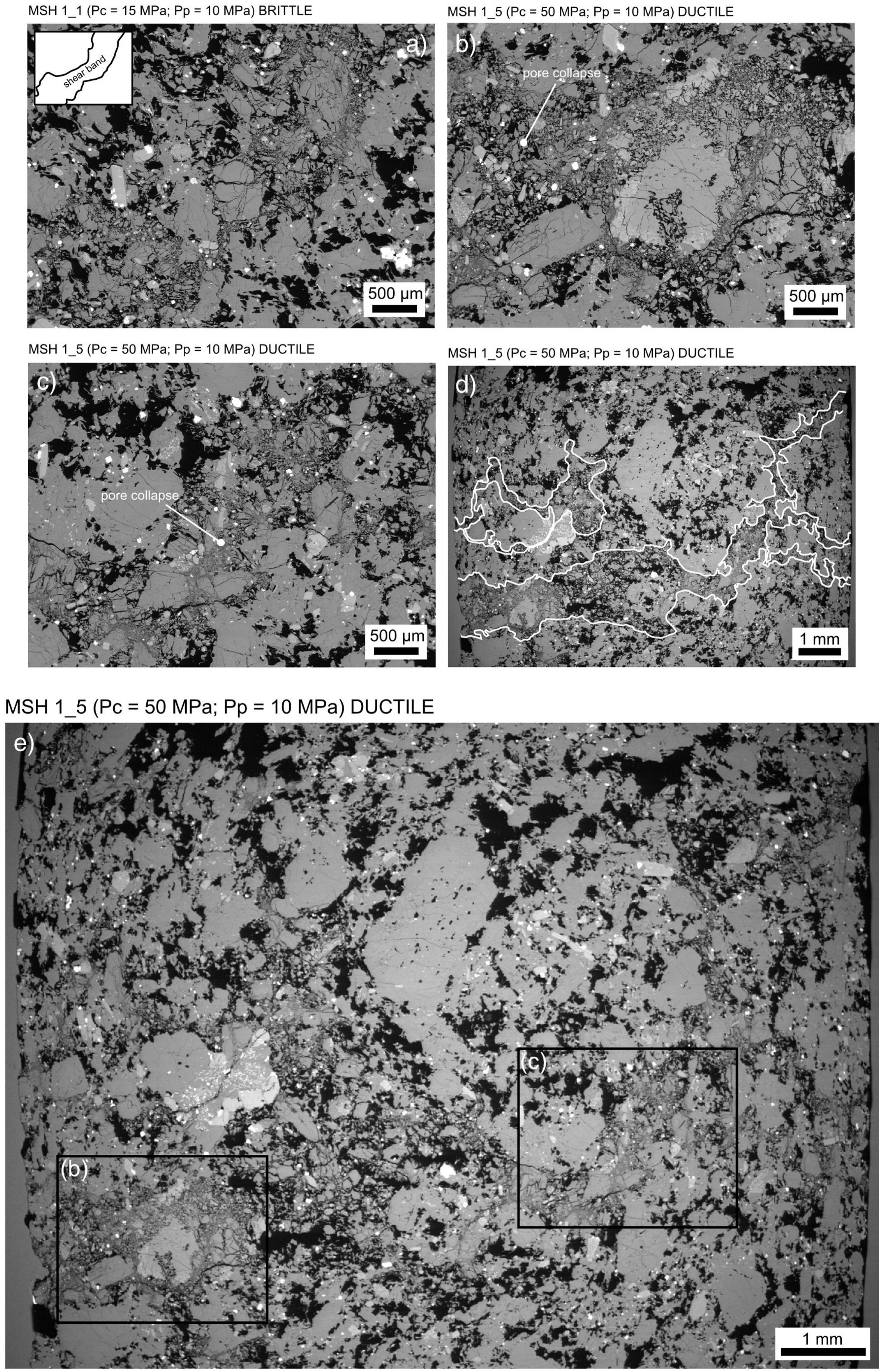

Please cite this article as: Heap, M.J., et al., Mechanical behaviour of dacite from Mount St. Helens (USA): A link between porosity and lava dome extrusion mechanism (dome or spi..., J. Volcanol. Geotherm. Res. (2016), http://dx.doi.org/10.1016/j.jvolgeores.2016.10.015

permeability of rocks that lie below the porosity changepoint (i.e., below ~0.15; Fig. 8), since fluid flow relies on microcrack connections, but may not influence the permeability of those rocks above the changepoint (i.e., above ~0.15–0.16; Fig. 8), since fluid flow in these materials is facilitated by a well-connected pore network (Fig. 2).

5.2. Micromechanical mechanisms

Macroscopic mechanical behaviour of material is ultimately an expression of the operative deformation micromechanisms. On this basis we present SEM images of samples of MSH1 deformed in the brittle regime ($Peff = 10$ MPa) and the ductile regime ($Peff = 40$ MPa) (Fig. 9). The sample deformed in the brittle regime contains a wide (~1 mm) shear fracture zone (Fig. 9a)—also visible with the naked eye—that is orientated at ~30° to the maximum principal stress. The shear fracture contains broken glass and crystal fragments (Fig. 9a). The thickness of the shear fracture damage zone is likely a result of the additional post-failure axial strain (~1%) that was accommodated by sliding along the newly-formed fault plane. The thickness of this band, and the amount of gouge produced, are dependent on the post-failure axial strain (Kennedy and Russell, 2012). The sample deformed in the ductile regime contains anastomosing bands (i.e., localised) oriented subparallel to the maximum principal stress (Fig. 9d–e; the band shown in Fig. 9e is highlighted in Fig. 9d) consisting of collapsed pores (Fig. 9b–c). These bands are similar to those seen in porous (porosity ~0.19) andesite deformed at high effective pressure (Heap et al., 2015a). The deformation micromechanisms are microcracking and cataclastic pore collapse in the brittle and ductile regimes, respectively.

5.3. Failure envelopes for dacite

Triaxial deformation data at different effective pressures permit the construction of failure envelopes that can be summarised graphically as differential stress (Q) versus effective mean stress (P). The peak differential stress σ_p delineates the brittle failure envelope, while the differential stress at the onset of shear-enhanced compaction (C^*) constrains the ductile yield cap (Wong et al., 1997; Wong and Baud, 2012 and references therein). Therefore, a sample would be pre-failure if the stress state plots inside the failure envelope. If the state of stress plots the rock outside the failure envelope on the left hand side, the rock will fail in a brittle manner (shear fracture). By contrast, the rock will suffer a ductile mode of failure (cataclastic pore collapse) if it plots outside the failure envelope on the right hand side. Based on the sensitivity of failure in both the brittle and ductile regime on porosity, we only use data for those samples within a narrow porosity range to construct our failure envelopes (Fig. 10; Table 2). The datapoint at $Q = 0$ MPa marks the point of lithostatic inelastic compaction (measured during the hydrostatic experiment), and is termed P^* (Wong and Baud, 2012). Over the range of experimental conditions implemented in this study, a full failure envelope was obtained for MSH1; a ductile failure mode was only observed for MSH2 at Peff = 40 MPa (Fig. 10). The failure envelopes of MSH1 and MSH2 highlight that MSH2 is intact over a much wider range of pressure conditions, a consequence of its lower porosity.

The shape of the compactive yield envelope has been described as parabolic for porous sedimentary rocks (Wong and Baud, 2012 and references therein) and microcrack-free porous volcanic rocks (Zhu et al., 2011; Loaiza et al., 2012; Heap et al., 2015b). Although data are sparse, compactive yield envelopes for extrusive volcanic rocks containing a dual porosity of microcracks and pores have been observed to be linear (Heap et al., 2015a). To discuss the shape of the compactive yield envelope for MSH1, we compare our experimental data with the best-fit elliptical envelope defined by the following expression (Wong et al., 1997):

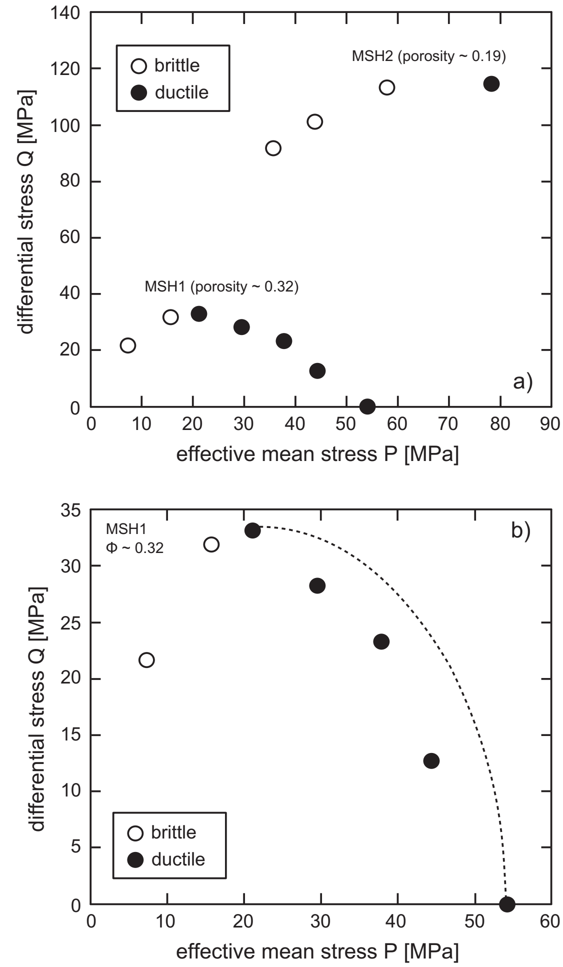

Fig. 10. (a) Failure envelopes for MSH1 and MSH2, plotted on a graph of differential stress Q against effective mean stress P. Failure in the brittle regime (white circles) is taken as the differential stress at the peak stress. In the ductile regime (black circles) the onset of inelastic pore collapse C^* delineates the yield envelope (see text for details). A sample is pre-failure when the state of stress plots inside the failure envelope; the sample has failed if the state of stress plots outside the failure envelope (brittle fracture on the left and cataclastic pore collapse on the right). (b) The failure envelope for MSH1 plotted with the best-fit parabolic yield envelope (Eq. (2)).

$$\frac{\left({}^{P}/_{P^*}-\gamma\right)^2}{(1-\gamma)^2}+\frac{\left({}^{Q}/_{P^*}\right)^2}{\delta^2}=1, \tag{2}$$

where γ and δ are the effective mean stress and the differential stress at the top of the ellipse normalised by P*, respectively. For MSH1, γ and δ were set at 0.4 and 0.62, respectively. Previous studies have found values of γ and δ to range between 0.5 and 0.7 (Wong et al., 1997). We find that the compactive yield envelope for the porous dacite (porosity ~0.32) studied here is linear in shape, not parabolic (Fig. 10b). As for the porous andesites of Heap et al. (2015a), we interpret the linear shape of the yield envelope as the result of the presence of microcracks (Fig. 2a).

If we plot the failure envelopes of this study alongside data from Kennedy et al. (2009), Smith et al. (2011) Kennedy and Russell (2012), and Kendrick et al. (2013) we notice that, in accordance with the Mohr-Coulomb criterion, the differential stress for brittle failure is a linear function of the effective mean stress (Fig. 11; Table 2). The data of Fig. 11 highlight that low-porosity dacite from MSH can be very strong. For example, the peak stress of dacite containing a porosity

Table 2
Summary of the mechanical data unique to this study, and those from Kennedy et al. (2009), Smith et al. (2011), Kennedy and Russell (2012), and Kendrick et al. (2013). T = temperature; *Pc* = confining pressure; *Pp* = pore pressure; *Peff* = effective pressure; C^* = the onset of shear-enhanced inelastic compaction; *P* = effective mean stress; P^* = the onset of inelastic hydrostatic compaction.

Reference	Location	Sample	Connected porosity	T (°C)	Strain rate (s^{-1})	*Pc* (MPa)	*Pp* (MPa)	*Peff* (MPa)	Peak differential stress Q (MPa)	Differential stress at C^* (MPa)	*P* (MPa)	P^* (MPa)
This study	1980 dome	MSH1 01	0.322	25	1.0×10^{-5}	15	10	5	31.8	–	15.6	–
This study	1980 dome	MSH1 02	0.321	25	1.0×10^{-5}	20	10	10	–	33.1	21.0	–
This study	1980 dome	MSH1 03	0.291	25	1.0×10^{-5}	30	10	20	–	44.7	34.9	–
This study	1980 dome	MSH1 04	0.303	25	1.0×10^{-5}	40	10	30	–	23.3	37.8	–
This study	1980 dome	MSH1 05	0.318	25	1.0×10^{-5}	50	10	40	–	12.8	44.3	–
This study	1980 dome	MSH1 06	0.333	25	1.0×10^{-5}	30	10	20	–	28.2	29.4	–
This study	1980 dome	MSH1 07	0.307	25	1.0×10^{-5}	0	0	0	21.7	–	7.2	–
This study	1980 dome	MSH1 08	0.367	25	1.0×10^{-5}	0	0	0	6.6	–	2.2	
This study	1980 dome	MSH1 09	0.312	25	1.0×10^{-5}	Hydro.	10	Hydro.	0	–	–	54
This study	1980 dome	MSH2 01	0.196	25	1.0×10^{-5}	15	10	5	91.8	–	35.6	–
This study	1980 dome	MSH2 02	0.184	25	1.0×10^{-5}	20	10	10	101.1	–	43.7	–
This study	1980 dome	MSH2 03	0.223	25	1.0×10^{-5}	0	0	0	37.0	–	12.3	–
This study	1980 dome	MSH2 04	0.199	25	1.0×10^{-5}	50	10	40	–	114.7	78.2	–
This study	1980 dome	MSH2 05	0.183	25	1.0×10^{-5}	30	10	20	113.5	–	57.8	–
This study	1980 dome	MSH2 06	0.179	25	1.0×10^{-5}	0	0	0		60.7	20.2	–
This study	1980 dome	MSH2 07	0.191	25	1.0×10^{-5}	40	10	30	164.1	–	84.7	–
This study	1980 dome	MSH2 08	0.197	25	1.0×10^{-5}	–	–	–	–	–	–	–
Kennedy et al. (2009)	2004–2008 spine	SH315-4B-02	0.075	25	1.0×10^{-4}	25	0	25	426.0	–	167.0	–
Kennedy et al. (2009)	2004–2008 spine	SH315-4B-03	0.073	25	1.0×10^{-4}	–	–	–	–	–	–	–
Kennedy et al. (2009)	2004–2008 spine	SH315-4B-04	0.076	25	1.0×10^{-4}	50	0	50	541.0	–	230.3	–
Kennedy et al. (2009)	2004–2008 spine	SH315-4B-05	0.077	25	1.0×10^{-4}	0	0	0	139.0	–	46.3	–
Kennedy et al. (2009)	2004–2008 spine	SH315-4B-06	0.075	25	1.0×10^{-4}	75	0	75	718.0	–	314.3	–
Smith et al. (2011)	27 Oct–1 Dec 2004	SH305-1	0.197	28	1.0×10^{-5}	10	0	10	67.0	–	32.3	–
Smith et al. (2011)	27 Oct–1 Dec 2004	SH305-1	0.197	850	1.0×10^{-5}	10	0	10	viscous	viscous	viscous	–
Smith et al. (2011)	27 Oct–1 Dec 2004	SH305-1	0.197	750	1.0×10^{-5}	0	0	0	43.0	–	14.3	–
Smith et al. (2011)	7–21 Dec 2004	SH306	0.121	25	1.0×10^{-5}	10	0	10	136.0	–	55.3	–
Smith et al. (2011)	7–21 Dec 2004	SH306	0.121	850	1.0×10^{-6}	10	0	10	133.0	–	54.3	–
Smith et al. (2011)	7–21 Dec 2004	SH306	0.121	850	1.0×10^{-5}	10	0	10	125.0	–	51.7	–
Smith et al. (2011)	7–21 Dec 2004	SH306	0.121	850	1.0×10^{-5}	0	0	0	103.0	–	34.3	–
Smith et al. (2011)	7–21 Dec 2004	SH306	0.121	900	1.0×10^{-5}	10	0	10	121.0	–	50.3	–
Smith et al. (2011)	15 Mar–5 Apr 2005	SH315-4	0.080	25	1.0×10^{-5}	10	0	10	199.0	–	76.3	–
Smith et al. (2011)	15 Mar–5 Apr 2005	SH315-4	0.080	850	1.0×10^{-5}	10	0	10	300.0	–	110.0	–
Smith et al. (2011)	Dec 2005–1 Jan 2006	SH325-1	0.095	25	1.0×10^{-5}	0	0	0	140.0	–	46.7	–
Smith et al. (2011)	Dec 2005–1 Jan 2006	SH325-1	0.095	25	1.0×10^{-6}	10	0	10	186.0	–	72.0	–
Smith et al. (2011)	Dec 2005–1 Jan 2006	SH325-1	0.095	25	1.0×10^{-5}	10	0	10	210.0	–	80.0	–
Smith et al.	Dec 2005–1 Jan	SH325-1	0.095	25	1.0 ×	10	0	10	197.0	–	75.7	–

(continued on next page)

Table 2 (*continued*)

Reference	Location	Sample	Connected porosity	T (°C)	Strain rate (s^{-1})	*Pc* (MPa)	*Pp* (MPa)	*Peff* (MPa)	Peak differential stress Q (MPa)	Differential stress at C^* (MPa)	*P* (MPa)	P^* (MPa)
(2011)	2006				10^{-5}							
Smith et al. (2011)	Dec 2005–1 Jan 2006	SH325-1	0.095	25	1.0×10^{-5}	10	0	10	165.0	–	65.0	–
Smith et al. (2011)	Dec 2005–1 Jan 2006	SH325-1	0.095	25	1.0×10^{-5}	10	0	10	168.0	–	66.0	–
Smith et al. (2011)	Dec 2005–1 Jan 2006	SH325-1	0.095	25	1.0×10^{-4}	10	0	10	202.0	–	77.3	–
Smith et al. (2011)	Dec 2005–1 Jan 2006	SH325-1	0.095	25	1.0×10^{-5}	30	0	30	286.0	–	125.3	–
Smith et al. (2011)	Dec 2005–1 Jan 2006	SH325-1	0.095	800	1.0×10^{-5}	0	0	0	101.0	–	33.7	–
Smith et al. (2011)	Dec 2005–1 Jan 2006	SH325-1	0.095	800	1.0×10^{-5}	10	0	10	213.0	–	81.0	–
Smith et al. (2011)	Dec 2005–1 Jan 2006	SH325-1	0.095	850	1.0×10^{-5}	0	0	0	93.0	–	31.0	–
Smith et al. (2011)	Dec 2005–1 Jan 2006	SH325-1	0.095	850	1.0×10^{-6}	10	0	10	194.0	–	74.7	–
Smith et al. (2011)	Dec 2005–1 Jan 2006	SH325-1	0.095	850	1.0×10^{-5}	10	0	10	253.0	–	94.3	–
Smith et al. (2011)	Dec 2005–1 Jan 2006	SH325-1	0.095	850	1.0×10^{-4}	10	0	10	285.0	–	105.0	–
Smith et al. (2011)	Dec 2005–1 Jan 2006	SH325-1	0.095	900	1.0×10^{-5}	0	0	0	137.0	–	45.7	–
Smith et al. (2011)	Dec 2005–1 Jan 2006	SH325-1	0.095	900	1.0×10^{-5}	10	0	10	190.0	–	73.3	–
Smith et al. (2011)	Dec 2005–1 Jan 2006	SH325-1	0.095	950	1.0×10^{-5}	0	0	0	140.0	–	46.7	–
Smith et al. (2011)	Dec 2005–1 Jan 2006	SH325-1	0.095	970	1.0×10^{-5}	0	0	0	90.0	–	30.0	–
Smith et al. (2011)	1 Apr 2006	SH328	0.103	25	1.0×10^{-5}	10	0	10	212.0	–	80.7	–
Smith et al. (2011)	1 Apr 2006	SH328	0.103	850	1.0×10^{-5}	10	0	10	225.0	–	85.0	–
Kennedy and Russell (2012)	2004–2008 spine	SH308-3-07	0.061	25	1.0×10^{-4}	0	0	0	138.0	–	46.0	–
Kennedy and Russell (2012)	2004–2008 spine	SH308-3-04	0.058	25	1.0×10^{-4}	25	0	0	408.0	–	161.0	–
Kennedy and Russell (2012)	2004–2008 spine	SH308-3-01	0.058	25	1.0×10^{-4}	25	0	0	377.0	–	150.7	–
Kennedy and Russell (2012)	2004–2008 spine	SH308-3-05	0.062	25	1.0×10^{-4}	50	0	0	538.0	–	229.3	–
Kennedy and Russell (2012)	2004–2008 spine	SH308-3-03	0.059	25	1.0×10^{-4}	75	0	0	722.0	–	315.7	–
Kendrick et al. (2013)	7–21 December 2004	SH306-1	0.121	25	1.0×10^{-5}	0	0	0	73.4	–	24.5	–
Kendrick et al. (2013)	15 March–5 April 2005	SH315-4	0.080	25	1.0×10^{-5}	0	0	0	82.6	–	27.5	–
Kendrick et al. (2013)	5 December 2005–1 January 2006	SH325-1	0.095	25	1.0×10^{-5}	0	0	0	94.6	–	31.5	–
Kendrick et al. (2013)	1 April 2006	SH328-1	0.103	25	1.0×10^{-5}	0	0	0	93.2	–	31.1	–
Kendrick et al. (2013)	Pine Creek Period	P07-3-1	0.212	25	1.0×10^{-5}	0	0	0	21.3	–	7.1	–
This study	2004–2008 spine	SH308-3-02	0.074	25	1.0×10^{-4}	25	0	25	333.0	–	136.0	–
This study	2004–2008 spine	SH308-3-06	0.055	25	1.0×10^{-4}	25	0	25	657.0	–	294.0	–
This study	2004–2008 spine	SH308-3-08	0.064	25	1.0×10^{-4}	25	0	25	582.0	–	269.0	–
This study	2004–2008 spine	SH3172A1-09	0.178	25	1.0×10^{-4}	25	0	25	153.1	–	76.0	–
This study	2004–2008 spine	SH3172A1-10	0.174	25	1.0×10^{-4}	25	0	25	162.7	–	79.2	–
This study	2004–2008 spine	SH-EN-09-09	0.082	1000	1.0×10^{-4}	0	0	0	69.0	–	23.0	–

of 0.06 was 722 MPa at Peff = 75 MPa (Kennedy and Russell, 2012). Another global observation is that the majority of experiments performed on samples of MSH were brittle (Fig. 11); this is largely of function of the low porosity and highly crystallised nature of the rocks forming the 2004–2008 spines (Kennedy et al., 2009; Kennedy and Russell, 2012; Smith et al., 2011; Kendrick et al., 2013; Table 2). The data of Fig. 11 include experiments performed on rocks preserving different porosities, deformed at different temperatures, and at different strain rates, factors known to influence the mechanical behaviour and failure mode of rocks (Paterson and Wong, 2005). In the following sections we will use these data to review and explore the role of porosity, strain rate, and temperature on the mechanical behaviour and failure mode of dacite from MSH.

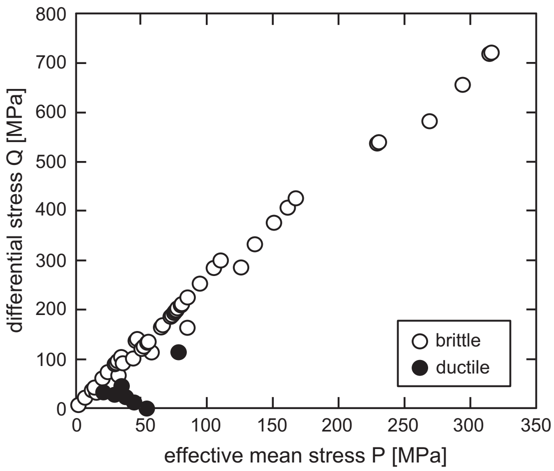

Fig. 11. Failure envelopes for dacite from MSH, plotted on a graph of differential stress *Q* against effective mean stress *P*. Data from this study and from Kennedy et al. (2009), Smith et al. (2011), Kennedy and Russell (2012), and Kendrick et al. (2013). Failure in the brittle regime (experiments denoted by white circles) is the differential stress at the peak stress. In the ductile regime (experiments denoted by black circles) the onset of inelastic pore collapse C^* delineates the yield envelope (see text for details).

5.4. Porosity as a control on mechanical behaviour and failure mode of dacite

Porosity is known to influence the strength of volcanic rocks in the brittle regime (Al-Harthi et al., 1999; Kennedy et al., 2009; Heap et al., 2014a, 2014b; Rotonda et al., 2014; Schaefer et al., 2015; Zhu et al., 2016) and their failure mode (i.e., brittle or ductile; Kennedy et al., 2009; Heap et al., 2015a; Zhu et al., 2016). We find that high-porosity dacite can be ductile at room temperature when deformed at elevated pressure (Fig. 10), in accordance with previous triaxial deformation studies on high-porosity dacite from Augustine volcano (Kennedy et al., 2009) and other volcanic rocks such as basalt (Adelinet et al., 2013; Zhu et al., 2016), tuff (Zhu et al., 2011), and andesite (Heap et al., 2015a). We performed two ancillary triaxial experiments to further explore the notion that porosity is a key parameter in dictating the failure mode of dacite. These experiments were performed on samples of the 2004–2008 MSH spines and are special in that they preserve a higher residual porosity (porosity = 0.18 and 0.17; Table 2) than previously-studied dacites from the 2004–2008 eruption. These triaxial experiments were performed at room temperature on dry cylindrical samples (diameter of 25.4 mm and cut and precision-ground to a length of about 50 mm) at a *Pc* of 25 MPa in the Large Sample Rig (LSR; see Austin et al., 2005) triaxial rock press at the Centre for Experimental Studies of the Lithosphere (CESL). The samples were deformed at a constant strain rate of 10^{-4} s^{-1}. The stress-strain curves for these experiments, together with a low-porosity sample from the 2004–2008 spine (from Kennedy et al., 2009), are presented in Fig. 12. We find that the high-porosity samples from the 2004–2008 spine are still brittle (the curves display strain-softening), but are much closer to the brittle-ductile transition than the low-porosity dacite (Fig. 12). From the available data, the transition from brittle to ductile behaviour at depths relevant for a volcanic edifice is encountered in dacitic rock containing a porosity of ~0.2. However, while it is clear that porosity exerts a first-order control on the brittle-ductile transition in volcanic rocks, there is still much to learn as to the influence of pore size, pore shape, and pore size distribution (as discussed in Heap et al., 2015a).

To assess the influence of porosity on brittle strength, we restrict ourselves to room temperature uniaxial data at a constant strain rate of 10^{-5} s^{-1} (data from this study, Smith et al., 2011, and Kendrick et al., 2013). Uniaxial data has the advantage that we can explore the mechanics of failure using 2D micromechanical models (Sammis and Ashby, 1986; Heap et al., 2016). Uniaxial compressive strength (*UCS*) as a function of connected porosity (ϕ) is presented as Fig. 13 and shows that strength decreases as porosity increases (as found previously by many authors; e.g., Al-Harthi et al., 1999: Heap et al., 2014a, 2014b; Schaefer et al., 2015). The micromechanical model of Sammis and Ashby (1986) is a 2D model consisting of an elastic medium populated by circular pores of uniform radius *r*. When the applied stress reaches a critical value equal to or exceeding the fracture toughness (K_{IC}), microcracks propagate from the pore walls parallel to the direction of the maximum principal stress to a distance l. When these microcracks reach a certain length, they can interact thereby increasing local tensile stresses. These microcracks eventually coalesce and conspire to induce the macroscopic failure of the elastic medium. This micromechanical model has been used to describe the mechanical behaviour of sedimentary rocks (Baud et al., 2014) and volcanic materials (Zhu et al., 2011; Vasseur et al., 2013; Heap et al., 2014a, 2015c). Zhu et al. (2010) derived an analytical approximation for the micromechanical model of Sammis and Ashby (1986) in the case of uniaxial compression:

$$UCS = \frac{1.325}{\phi^{0.414}} \frac{K_{IC}}{\sqrt{\pi r}}. \tag{3}$$

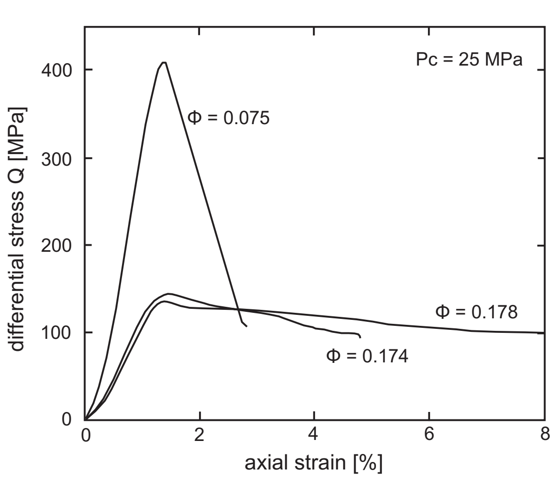

Fig. 12. Stress-strain curves for 2004–2008 spine samples (dry) deformed at a confining pressure of 25 MPa. The connected porosity of each sample is labelled next to the relevant curve.

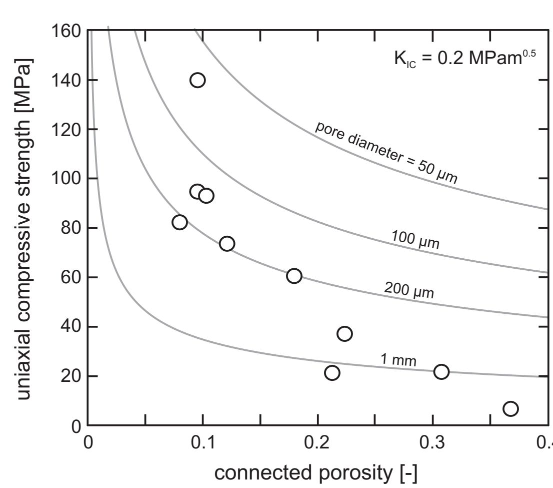

Fig. 13. Uniaxial compressive strength (UCS) as a function of connected porosity for dacite from MSH. Data from this study, Smith et al. (2011), and Kendrick et al. (2013). Grey curves are modelled curves using the analytical approximation of Sammis and Ashby's (1986) micromechanical model (Eq. (3)) (see text for details).

Please cite this article as: Heap, M.J., et al., Mechanical behaviour of dacite from Mount St. Helens (USA): A link between porosity and lava dome extrusion mechanism (dome or spi..., J. Volcanol. Geotherm. Res. (2016), http://dx.doi.org/10.1016/j.jvolgeores.2016.10.015

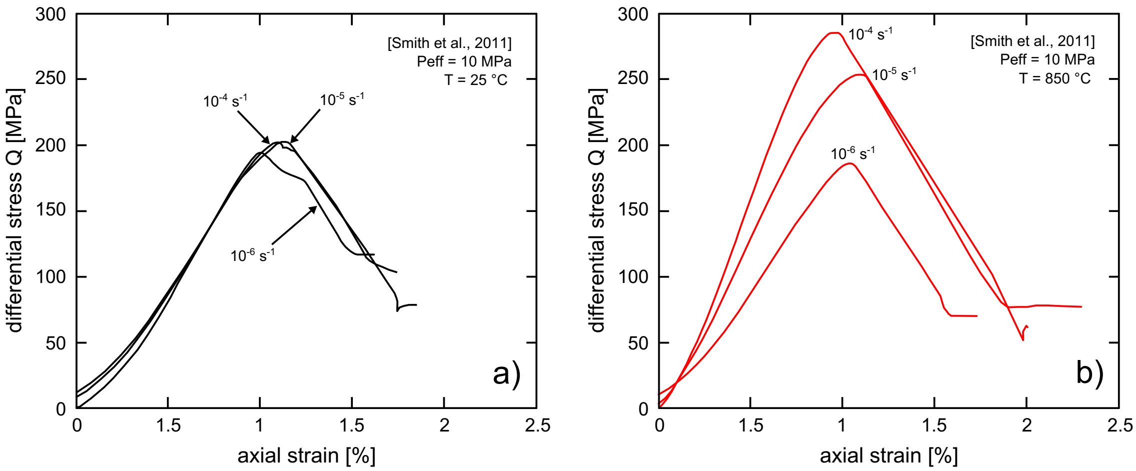

Fig. 14. The influence of strain rate on strength and failure mode of dacite from MSH (all data from Smith et al., 2011). (a) Stress-strain curves for three room-temperature triaxial experiments performed at different constant strain rates (indicated next to each curve). (b) Stress-strain curves for three high-temperature (850 °C) triaxial experiments performed at different constant strain rates (indicated next to each curve).

Fracture toughness K_{IC} tests on porous dacite from Mount Unzen yielded values from ~1.5 to ~0.3 MPam$^{0.5}$ (Scheu et al., 2008). These K_{IC} data, however, are for the bulk rock, cracks on the lengthscale considered here—the microscale—will propagate through the phenocrysts and groundmass (and thus values K_{IC} for the individual minerals may be more representative) or, and more likely, along weak crystal/particle boundaries. As a result, values of K_{IC} best suited for the model of Eq. (2) are likely lower than those values determined for the bulk rock (as discussed in Heap et al., 2016; see also Tromans and Meech, 2002). Indeed, a low value of $K_{IC} = 0.15$ MPam$^{0.5}$ well described the strength of variably-porous (porosity from ~0.07 to ~0.25) dacitic block-and-ash flow data from Mt. Meager, Canada (Heap et al., 2015c). We assume here that $K_{IC} = 0.2$ MPam$^{0.5}$ and plot modelled strength curves for pore diameters between 50 μm and 1 mm (Fig. 13). We find that the data cannot be described by a single modelled curve (Fig. 13); a likely consequence of the changing pore size as porosity is decreased (as confirmed by microstructural observations; Fig. 2). A recent study has highlighted an important role for crystal content on the brittle strength of volcanic rocks (Heap et al., 2016), and provided a modified version of the analytical approximation for Sammis and Ashby's (1986) model that accounts for the weakening influence of crystals. However, while we can estimate the crystal content of the rocks studied herein, the phenocryst content of the samples from Smith et al. (2011) and Kendrick et al. (2013) are not reported. Therefore, while we can conclude that porosity exerts a first-order control on brittle strength, other factors such as pore size, pore shape, and crystal content likely play an influential role.

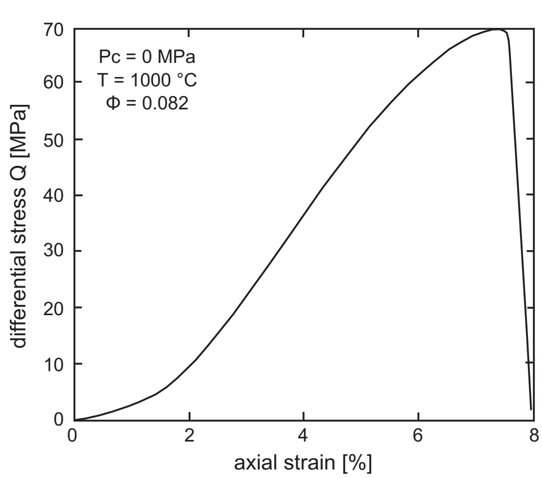

Fig. 15. Stress-strain curve for a 2004–2008 spine sample (dry) deformed under uniaxial conditions at a temperature of 1000 °C.

5.5. Strain rate as a control on mechanical behaviour and failure mode of dacite

The influence of strain rate on the brittle strength of dacite from MSH is presented in Fig. 14 (data from Smith et al., 2011). The data show that strain rate does not influence strength at room temperature between the strain rates of 10^{-6} and 10^{-4} s^{-1} (Fig. 14a; Table 2), in accordance with other studies on porous rocks in the brittle field (Paterson and Wong, 2005). Since the samples were dry, time-dependent deformation mechanisms such as stress corrosion (Brantut et al., 2013) were unlikely to have measurably reduced the strength at room temperature at the studied strain rates. However, strain rate is seen to influence strength at higher temperature (850 °C) (Fig. 14b). Strength is reduced from 285 MPa at a strain rate of 10^{-4} s^{-1} to 253 and 194 at strain rates of 10^{-5} and 10^{-6} s^{-1}, respectively (Fig. 14b; Table 2). While the viscous deformation of the melt phase could account for some of the weakening as strain rate is lowered, we highlight that the glass content of these samples was estimated at 2 vol.% (Smith et al., 2011). It is likely, therefore, that the rate of subcritical crack growth was accelerated at 850 °C; the rate of stress corrosion cracking, for example, is known to be significantly increased at elevated temperatures (Kranz et al., 1982).

At temperatures above the appropriate *Tg*, strain rate has been shown to have a profound influence on the failure mode (brittle or ductile) of glass-rich volcanic materials (e.g., Cordonnier et al., 2012; Lavallée et al., 2013). However, decreases in strain rate are unlikely to promote a ductile response in volcanic rocks that are completely crystallised or those below the appropriate *Tg* (Paterson and Wong, 2005). However, firm conclusions cannot be drawn due to lack of pertinent data concerning the influence of strain rate on the failure mode of volcanic rocks.

5.6. Temperature as a control on mechanical behaviour and failure mode of dacite

To assess the role of temperature on the mechanical behaviour of dacite, we will consider data from one block of MSH dacite (porosity = 0.095; glass content = 2 vol.%), deformed at the same effective pressure (*Peff* = 10 MPa) and the same strain rate (strain rate = 10^{-5} s^{-1}) (data from Smith et al., 2011). Data under these conditions at room temperature yielded strengths between 165 and 210 MPa (Table 2); strengths at 800, 850, and 900 °C were 213, 253, and 190 MPa, respectively. Based on the scatter in these data, we must conclude that temperature does not have a significant impact on brittle strength and this probably reflects the highly crystallised nature of the rock. If we consider a rock with a slightly higher glass content (porosity = 0.121; glass content = 10 vol.%), we notice that strength is reduced from 136 MPa at room temperature to 133 and 121 MPa at temperatures of 850 and 900 °C, respectively (Table 2). This modest, but systematic, weakening as temperature is increased may be the consequence of the viscous deformation of the melt phase (i.e., glass raised above its *Tg*), which will be enhanced at higher temperatures due to the temperature dependence of viscosity (e.g., Dingwell et al., 1996).

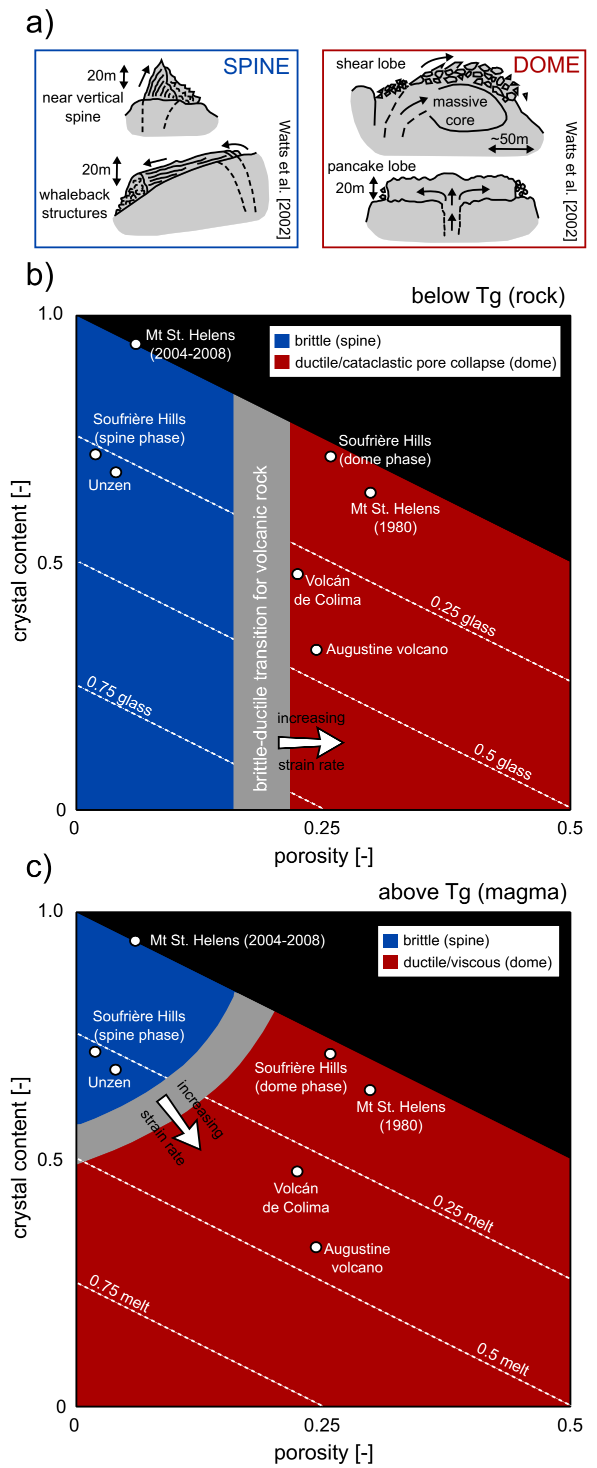

Fig. 16. (a) Cartoons of spine, whaleback, shear lobe, and pancake lobe (redrawn from Watts et al., 2002). (b and c) Conceptual diagrams showing the anticipated roles of porosity and crystal content on the deformation behaviour (brittle or ductile, spine or blocky dome) of volcanic rocks (b) and magma (c). The componentry of the volcanic materials are represented here as porosity (x-axis), crystal content (y-axis), and glass/melt fraction (dashed lines). Although we are aware that the erupted material at a volcano can vary significantly, we have highlighted an approximate position for MSH (data from Kennedy et al., 2009 and this study), Augustine volcano (Kennedy et al., 2009), Soufrière Hills volcano (Melnik and Sparks, 2002), Mount Unzen (Cordonnier et al., 2009), and Volcán de Colima (Lavallée et al., 2012).

The failure mode of dacite from MSH was staunchly brittle, even at temperatures between 800 and 900 °C (Smith et al., 2011). A transition from brittle to ductile behaviour as temperature is increased above the *Tg* of the glass phase may be anticipated in rocks that contain a more substantial glass phase; the dacites deformed from the 2004–2006 spine were however nearly completely crystallised (Smith et al., 2011). To reinforce the notion that high temperature does not alter the failure mode of highly crystallised dacite from MSH, we offer an additional uniaxial experiment on a sample collected from the 2004–2008 spine (porosity = 0.08) at a temperature of 1000 °C (Table 2). The experiment was performed on a dry cylindrical sample (12.7 mm in diameter and 25.4 mm in length) in the Volcanology Deformation Rig (VDR; see Quane et al., 2004) at CESL at a constant strain rate of 10^{-4} s^{-1}. The stress-strain curve for the experiment is presented in Fig. 15 and shows that the sample fails in a brittle manner in spite of the high temperature (i.e., above the eruptive temperature).

5.7. Implications for Mount St. Helens and dacitic volcanoes worldwide

5.7.1. Modelling outgassing and volcanic unrest

Models of volcano outgassing (Collombet, 2009; Collinson and Neuberg, 2012) and unrest (Hurwitz et al., 2007; Todesco et al., 2010) are sensitive to estimates of permeability for volcanic materials. Our porosity-permeability compilation for MSH (Fig. 8; Table 1) shows that the permeability of dacite from MSH can vary by almost seven orders of magnitude. This variation is attributed to the array of microstructural and textural differences between typical edifice-forming (i.e., explosive and effusive) dacites. We note here that laboratory measurements of permeability are, however, inherently scale-dependent (Brace, 1984; Clauser, 1992; Neuman, 1994): the permeability of low-permeability samples measured in the laboratory will be higher when the lengthscale of consideration is longer than the macrofracture spacing (Heap and Kennedy, 2016). The wide range of permeability for edifice-building rocks at MSH highlights the challenges for the construction of more complex models for volcanic outgassing and unrest.

5.7.2. Structural stability

Volcanic edifices are heterogeneous structures comprising rocks with diverse origins and disparate properties. Their growth is predicated by the progressive accumulation of the products of explosive and effusive eruptions (Odbert et al., 2015), as well as the near-surface intrusion of magma (Biggs et al., 2010). The structural stability of a volcanic edifice is a function of the physical properties (such as strength) and mechanical behaviour of the assembled materials (Voight and Elsworth, 1997; Voight, 2000; Watters et al., 2000; Thomas et al., 2004; Apuani et al., 2005). Mechanical failure of the edifice poses two main hazards. First, flank collapse can initiate potentially catastrophic and fatal rock/debris avalanches and tsunamis (Siebert, 1996; McGuire, 1996; Keating and McGuire, 2000; Voight et al., 2002). Second, flank collapse can depressurise deep magma and trigger highly explosive and sustained eruptions. The latter scenario is exemplified by the devastating Plinian eruption of MSH on the 18th of May 1980 (Lipman and Mullineaux, 1981).

The values of strength provided by this study and others (Table 2), considered here to be representative of edifice-forming dacites, permit the estimation of a rock mass rating (RMR) for dacite-dominated edifices such as MSH, provided that other parameters—such as the fracture spacing—are known (e.g., Watters et al., 2000; Thomas et al., 2004; Apuani et al., 2005). While measurements of strength in the laboratory are inherently scale-dependent (e.g., Schultz, 1996), RMR estimates provide values of strength beyond the laboratory lengthscale and are commonly used to assess volcano stability (e.g., Watters et al., 2000; Thomas et al., 2004; Apuani et al., 2005).

Although many of the dacites at MSH preserve low porosities, and are therefore strong (Table 2), we have shown that high-porosity (porosity ~0.32) dacite can be weak (UCS ~6 MPa). Previous studies of volcanic flank instability have highlighted an important role for a weak basal layer in governing flank spreading and destabilisation (e.g., Andrade and van Wyk de Vries, 2010). Layers of rock that preserve high porosities (such as high-porosity dome rock or pumice) could serve as the focus of instability in dacitic stratovolcanoes, driving gravitational spreading.

Catastrophic flank collapse is often thought to be triggered by increases in pore pressure caused by, for example, dyke intrusion (Elsworth and Voight, 1996; Elsworth and Day, 1999) or hydrothermal pressurisation (Reid, 2004). In accordance with previous studies, we have shown here that dacite in the brittle regime is weaker at lower effective pressures (Fig. 5a; Table 2). If effective pressure is defined simply as the confining pressure minus the pore pressure, then increases in pore pressure will result in a reduction in brittle strength (see also Farquharson et al., 2016a) thus jeopardising slope stability. Increases in pore pressure also reduce the normal stress acting on pre-existing discontinuities; fault movement can result in bulging, intense fracturing, and landsliding within the flanks that greatly destabilise the volcano (Lagmay et al., 2000).

5.7.3. Extrusion mechanism (dome or spine)

Triaxial deformation experiments on representative rocks collected from the 2004–2008 spine-forming eruption and the 1980 dome-forming eruption at MSH highlight their disparate failure modes (Table 2). While the majority of samples from the 2004–2008 spines behaved in a brittle manner, even over a broad range of temperatures and strain rates (Figs. 11 and 14; Kennedy et al., 2009; Smith et al., 2011; Kennedy and Russell, 2012; Table 2), high-porosity samples from the 1980 dome deformed in a ductile manner, even at low pressure (shallow depths) and room temperature (Fig. 4b; Table 2). The difference in failure mode (brittle versus ductile) reflects the residual porosity of extruded material which itself may be indicative of ascent rate, and therefore time for outgassing, cooling, and crystallisation. Ascent rates inferred for the 1980–1986 eruptive activity are between 15 and 66 m/h (Rutherford and Hill, 1993), much faster than those estimated for the 2004–2008 activity, estimated to be ~0.2–0.5 m/h (Cashman et al., 2008; Vallance et al., 2008). The slow ascent rate during the 2004–2008 eruption formed dacites that are typically low-porosity that are highly crystallised and therefore preserve a low glass content; these lavas may also extrude close to or below their Tg. The physical attributes of these materials (crystallised and low-porosity), and the conditions under which they are extruded (near or below Tg), suggest that excursions from the brittle deformation window are extremely unlikely. By contrast, the fast ascent rate during the 1980–1986 eruption produced highly porous, melt-bubble mixtures with subordinate crystal contents; these materials are also likely to erupt at temperatures above Tg. The physical attributes of these magmas (melt-rich and high-porosity), and the conditions under which they are extruded (above Tg), suggest that excursions from the ductile deformation window are unlikely. Deformation of these materials will be likely accommodated by viscous flow where above Tg or by cataclastic pore collapse where below Tg.

The extrusion of spines and whalebacks typically occurs along pronounced conduit-margin faults (i.e., brittle deformation). Indeed, spine extrusion at MSH was linked to co-seismic slip along small displacement (~5 mm) faults at the conduit margins (Iverson et al., 2006; Pallister et al., 2008; Kendrick et al., 2014) and the spines featured a 1–3 m thick enveloping carapace of faulted rock comprising striated fault gouge, indurated cataclasites, and angular breccia (Dzurisin et al., 2005; Cashman et al., 2008; Kennedy et al., 2009; Kennedy and Russell, 2012; Pallister et al., 2013). Carapaces of fault rocks and seismicity were also observed during recent spine growth at Mount Unzen (Nakada et al., 1999; Cordonnier et al., 2009; Hornby et al., 2015; Lamb et al., 2015) and Soufrière Hills volcano (Sparks et al., 2000; Melnik and Sparks, 2002). The extrusion of these gouge-rich spines along conduit margin faults is clearly an expression of pronounced strain localisation (i.e., a brittle failure mode). Thus, we infer that the formation of spines and whaleback structures is possible only if rising magmas can readily lose their porosity and, simultaneously, crystallise or cool below Tg. These events allow the system to behave in a brittle manner where strain is accommodated by a localised shear fault, resulting in spines and whalebacks. We speculate that magma will extrude as blocky domes and lobes in situations where there is a high residual porosity, as was the case for the 1980 dome (Table 2). This is because high-porosity materials are likely ductile (i.e., shear fractures do not form) even at room temperature (Fig. 4; Table 2). Our hypothesis is also supported, empirically, by the apparent connection between porosity (Melnik and Sparks, 2002), discharge rate, and lava extrusion mechanism (Watts et al., 2002) documented by detailed field observations at Soufrière Hills volcano.

The compiled experimental data allow us to construct tentative crystal content-porosity maps for brittle (spine/whaleback) versus ductile (blocky dome/lobe) behaviour (Fig. 16). We have prepared maps for two scenarios: below Tg (i.e., rock; Fig. 16b) and above Tg (i.e., magma; Fig. 16c). Below Tg (Fig. 16b), our experimental data help constrain a boundary (grey field) between brittle and ductile behaviour for rock that is governed solely by the residual porosity. Based on published experiments and data here, ductile behaviour of volcanic rock requires a residual porosity >0.2. We anticipate no influence of glass versus crystal content on brittle versus ductile behaviour in volcanic materials below Tg, and that the brittle field will expand at faster strain rates (Fig. 16b). Below Tg, the porosity-crystal content space for spine extrusion is large (Fig. 16b). Above Tg (Fig. 16c), volume fraction of glass/melt plays a crucial role in expanding the window for ductile deformation and therefore dome/lobe extrusion. Brittle behaviour is limited to low-porosity magmas (porosity <0.2, since volcanic materials are ductile even at room temperature above a porosity of ~0.2) with very high crystal contents. We denote this boundary by the grey curvilinear band on Fig. 16c; we note that faster strain rates will shift this conceptual boundary to expand the brittle domain (Dingwell, 1996). Fig. 16c shows that the brittle or spine-extrusion field becomes very small above Tg and offers an explanation as to why they are not frequently observed in nature. Although we are aware that the crystal content and porosity of volcanic materials can vary significantly within the same volcanic system (e.g., Farquharson et al., 2015), we have highlighted an approximate position of several dacitic and andesitic volcanoes in our crystal content-porosity maps (Fig. 16b–c). We offer approximate positions for MSH (data from Kennedy et al., 2009 and this study), Augustine volcano (Kennedy et al., 2009), Soufrière Hills volcano (Melnik and Sparks, 2002), Mount Unzen (Cordonnier et al., 2009), and Volcán de Colima (Mexico; Lavallée et al., 2012) (Fig. 16b–c). Material representative of the spines of MSH, Mount Unzen, and Soufrière Hills volcano (spine phase) are low-porosity and highly crystallised and plot within the brittle/spine domain on both of our crystal content-porosity maps (below and above Tg; Fig. 16b–c). Dome-forming volcanoes, such as Augustine volcano and Volcán de Colima, typically extrude porous materials and plot within the ductile/dome domain on our crystal content-porosity maps (Fig. 16b–c).

6. Concluding remarks

Triaxial deformation experiments on representative rocks collected from the 2004–2008 spine-forming eruption and the 1980 dome-forming eruption at MSH show that the dense 2004–2008 dacites are staunchly brittle in their failure mode, while the high-porosity 1980 dacites deform ductilely. We interpret this as a consequence of the time available for outgassing, cooling, and crystallisation, a function of the magma ascent rate. The dacites from the 1980 eruption ascended quickly (15–66 m/h; Rutherford and Hill, 1993), leaving limited time for outgassing, cooling, and crystallisation: these dacites are high-porosity with low crystal contents, factors that favour ductile deformation. The dacites from the 2004–2008 eruption ascended slowly (~0.2–0.5 m/h; Cashman et al., 2008; Vallance et al., 2008), leaving ample time for outgassing, cooling, and crystallisation: these dacites are low-porosity with very high crystal contents, and low glass content, factors that favour brittle deformation. Since the extrusion of spines and whalebacks requires faults (i.e., brittle deformation) at the conduit margin-wall rock interface, we suggest here that residual porosity and crystallinity, functions of the magma ascent rate, are important factors governing lava dome extrusion mechanism (blocky dome or spine). A crystal content-porosity map for brittle (spine) versus ductile (blocky dome) behaviour demonstrates that the window for brittle deformation is small and offers an explanation as to why spine and whaleback structures are relatively rare in nature.

Acknowledgements

Funding was provided by an NSERC Discovery grant to J.K. Russell and L. Kennedy. J.K. Russell also acknowledges funding through the NSERC Discovery Accelerator Supplement program. We thank Thierry Reuschlé, Patrick Baud, Luke Griffiths, Jamie Farquharson, Edward Nelles, Stephan Kolzenburg, Betsy Friedlander, and Alex Kushnir. The first author also acknowledges an Initiative d'Excellence (IDEX) Attractivité grant ("VOLPERM"), funded by the University of Strasbourg. Gilles Morvan is thanked for SEM assistance. The photograph of the 1980 dome is used here with permission from Gary Braasch (Copyright © 1980 Gary Braasch Photography). We were saddened to hear of the untimely passing of Gary in March of this year. We are grateful for the constructive reviews of one anonymous reviewer and Nick Varley, and the editorial assistance of Alessandro Aiuppa.

References

Adelinet, M., Fortin, J., Schubnel, A., Guéguen, Y., 2013. Deformation modes in an Icelandic basalt: from brittle failure to localized deformation bands. J. Volcanol. Geotherm. Res. 255, 12–25.

Al-Harthi, A.A., Al-Amri, R.M., Shehata, W.M., 1999. The porosity and engineering properties of vesicular basalt in Saudi Arabia. Eng. Geol. 54, 313–320.

Andrade, S.D., van Wyk de Vries, B., 2010. Structural analysis of the early stages of catastrophic stratovolcano flank-collapse using analogue models. Bull. Volcanol. 72, 771–789.

Apuani, T., Corazzato, C., Cancelli, A., Tibaldi, A., 2005. Physical and mechanical properties of rock masses at Stromboli: a dataset for volcano instability evaluation. Bull. Eng. Geol. Environ. 64, 419–431.

Armienti, P., 2008. Decryption of igneous rock textures: crystal size distribution tools. Rev. Mineral. Geochem. 69 (1). http://dx.doi.org/10.2138/rmg.2008.69.16.

Austin, N.J., Kennedy, L.A., Logan, J.M., Rodway, R., 2005. Textural controls on the brittle deformation of dolomite: the transition from brittle faulting to cataclastic flow. In: Gapais, D., Brun, J.P., Cobbold, P.R. (Eds.), Deformation Mechanisms, Rheology and Tectonics: From Minerals to the Lithosphere 243. Geological Society of London, Special Publication, pp. 51–66.

Ball, J.L., Calder, E.S., Hubbard, B.E., Bernstein, M.L., 2013. An assessment of hydrothermal alteration in the Santiaguito lava dome complex, Guatemala: implications for dome collapse hazards. Bull. Volcanol. 75:676. http://dx.doi.org/10.1007/s00445-012-0676-z.

Baud, P., Klein, E., Wong, T.-f., 2004. Compaction localization in porous sandstones: spatial evolution of damage and acoustic emission activity. J. Struct. Geol. 26, 603–624.

Baud, P., Wong, T.-f., Zhu, W., 2014. Effects of porosity and crack density on the compressive strength of rocks. Int. J. Rock Mech. Min. Sci. 67, 202–211.

Bauer, S.J., Friedman, M., Handin, J., 1981. Effects of water-saturation on strength and ductility of three igneous rocks at effective pressures to 50 MPa and temperatures to partial melting. The 22nd U.S. Symposium on Rock Mechanics (USRMS), June 29–July 2, 1981, Cambridge, MA.

Biggs, J., Mothes, P., Ruiz, M., Amelung, F., Dixon, T.H., Baker, S., Hong, S.-H., 2010. Stratovolcano growth by co-eruptive intrusion: the 2008 eruption of Tungurahua Ecuador. Geophys. Res. Lett. 37:21. http://dx.doi.org/10.1029/2010GL044942.

Blundy, J., Cashman, K.V., 2001. Ascent-driven crystallisation of dacite magmas at Mount St Helens, 1980-1986. Contrib. Mineral. Petrol. 140, 631–650.

Brace, W.F., 1984. Permeability of crystalline rocks: new in situ measurements. J. Geophys. Res. 89, 4327–4330.

Brantut, N., Heap, M.J., Meredith, P.G., Baud, P., 2013. Time-dependent cracking and brittle creep in crustal rocks: a review. J. Struct. Geol. 52, 17–43.

Calder, E.S., Lavallée, Y., Kendrick, J.E., Bernstein, M., 2015. Lava dome eruptions. In: Sigurdsson, H., Houghton, B., McNutt, S.R., Rymer, H., Stix, J. (Eds.), The Encyclopedia of Volcanoes. Elsevier Academic Press, pp. 343–362.

Cashman, K.V., Thornber, C.R., Pallister, J.S., 2008. From dome to dust: Shallow crystallization and fragmentation of conduit magma during the 2004–2006 dome extrusion of Mount St. Helens, Washington. In: Sherrod, D.R., Scott, W.E., Stauffer, P.H. (Eds.), A Volcano Rekindled: The First Years of Renewed Eruption at Mount St. Helens 2004–2006, U.S. Geological Survey Professional Paper 2007-XXXX.

Clauser, C., 1992. Permeability of crystalline rocks. Earth and Space Science News. 73, pp. 233–238.

Collinson, A.S.D., Neuberg, J., 2012. Gas storage, transport and pressure changes in an evolving permeable volcanic edifice. J. Volcanol. Geotherm. Res. 243-244, 1–13.

Collombet, M., 2009. Two-dimensional gas loss for silicic magma flows: toward more realistic numerical models. Geophys. J. Int. 177, 309–318.

Cordonnier, B., Hess, K.-U., Lavallée, Y., Dingwell, D.B., 2009. Rheological properties of dome lavas: case study of Unzen volcano. Earth Planet. Sci. Lett. 279, 263–272.

Cordonnier, B., Caricchi, L., Pistone, M., Castro, J., Hess, K.-U., Gottschaller, S., Manga, M., Dingwell, D.B., Burlini, L., 2012. The viscous-brittle transition of crystal-bearing silicic melt: direct observation of magma rupture and healing. Geology 40, 611–614.

Dingwell, D.B., 1996. Volcanic dilemma–flow or blow? Science 273, 1054–1055.

Dingwell, D.B., Romano, C., Hess, K.-U., 1996. The effect of water on the viscosity of a haplogranitic melt under PTX conditions relevant to silicic volcanism. Contrib. Mineral. Petrol. 124, 19–28.

Dzurisin, D., Vallance, J.W., Gerlach, T.M., Moran, S.C., Malone, S.D., 2005. Mount St. Helens reawakens. EOS Trans. Am. Geophys. Union 86, 25–29.

Elsworth, D., Voight, B., 1996. Evaluation of volcano flank instability triggered by dyke intrusion. Geol. Soc. Lond. Spec. Publ. 110, 45–53.

Elsworth, D., Day, S.J., 1999. Flank collapse triggered by intrusion: the Canarian and Cape Verde Archipelagoes. J. Volcanol. Geotherm. Res. 94, 323–340.

Evans, B., Frederich, J.T., Wong, T.-F., Duba, A.G., Durham, W.B., Handin, J., Wang, H.F., 1990. The brittle-ductile transition in rocks: recent experimental and theoretical progress. The Brittle-ductile Transition in rocks. The Heard volume, American Geophysical Union, Geophys Monograph 56, Washington.

Farquharson, I.J., Heap, M.J., Varley, N., Baud, P., Reuschlé, T., 2015. Permeability and porosity relationships of edifice-forming andesites: a combined field and laboratory study. J. Volcanol. Geotherm. Res. 297, 52–68.

Farquharson, I.J., Heap, M.J., Baud, P., Reuschlé, T., Varley, N., 2016a. Pore pressure embrittlement in a volcanic edifice. Bull. Volcanol. 78 (6).

Farquharson, J.I., Heap, M.J., Lavallée, Y., Baud, P., 2016b. Evidence for the development of permeability anisotropy in lava domes and volcanic conduits. J. Volcanol. Geotherm. Res. 323, 163–185.

Gaunt, H.E., Sammonds, P.R., Meredith, P.G., Smith, R., Pallister, J.S., 2014. Pathways for degassing during the lava dome eruption of Mount St. Helens 2004–2008. Geology http://dx.doi.org/10.1130/G35940.1.

Gaunt, H.E., Sammonds, P.R., Meredith, P.G., Chadderton, A., 2016. Effect of temperature on the permeability of lava dome rocks from the 2004–2008 eruption of Mount St. Helens. Bull. Volcanol. 78:30. http://dx.doi.org/10.1007/s00445-016-1024-5.

Geschwind, C.H., Rutherford, M.J., 1995. Crystallization of microlites during magma ascent: the fluid mechanics of 1980–1986 eruptions at Mount St Helens. Bull. Volcanol. 57, 356–370.

Heap, M.J., Lavallée, Y., Petrakova, L., Baud, P., Reuschlé, T., Varley, N., Dingwell, D.B., 2014a. Microstructural controls on the physical and mechanical properties of edifice-forming andesites at Volcán de Colima, Mexico. J. Geophys. Res. 119, 2925–2963.

Heap, M.J., Xu, T., Chen, C.-f., 2014b. The influence of porosity and vesicle size on the brittle strength of volcanic rocks and magmas. Bull. Volcanol. 76:856. http://dx.doi.org/10.1007/s00445-014-0856-0.

Heap, M.J., Farquharson, I.J., Baud, P., Lavallée, Y., Reuschlé, T., 2015a. Fracture and compaction of andesite in a volcanic edifice. Bull. Volcanol. 77:55. http://dx.doi.org/10.1007/s00445-015-0938-7.

Heap, M.J., Kennedy, B.M., Pernin, N., Jacquemard, L., Baud, P., Farquharson, I.J., Scheu, B., Lavallée, Y., Gilg, H.A., Letham-Brake, M., Mayer, K., Jolly, A.D., Reuschlé, T., Dingwell, D.B., 2015b. Mechanical behaviour and failure modes in the Whakaari (White Island volcano) hydrothermal system, New Zealand. J. Volcanol. Geotherm. Res. 295, 26–42.

Heap, M.J., Farquharson, I.J., Wadsworth, F.B., Kolzenburg, S., Russell, J.K., 2015c. Timescales for permeability reduction and strength recovery in densifying magma. Earth Planet. Sci. Lett. 429, 223–233.

Heap, M.J., Wadsworth, F.B., 2016. Closing an open system: pore pressure changes in permeable edifice rock at high strain rates. J. Volcanol. Geotherm. Res. 315, 40–50.

Heap, M.J., Kennedy, B.M., 2016. Exploring the scale-dependent permeability of fractured andesite. Earth Planet. Sci. Lett. 447, 139–150.

Heap, M.J., Wadsworth, F.B., Xu, T., Chen, C.-f., Tang, C.A., 2016. The strength of heterogeneous volcanic rocks: a 2D approximation. J. Volcanol. Geotherm. Res. 319, 1–11.

Heap, M.J., Byrne, P., Mikhail, S., 2017. Low surface gravitational acceleration of Mars results in a thick and weak lithosphere: implications for topography, volcanism, and hydrology. Icarus 281:103–114. http://dx.doi.org/10.1016/j.icarus.2016.09.003.

Hornby, A.J., Kendrick, J.E., Lamb, O.D., Hirose, T., De Angelis, S., von Aulock, F.W., Umakoshi, K., Miwa, T., Henton De Angelis, S., Wadsworth, F.B., Hess, K.-U., Dingwell, D.B., Lavallée, Y., 2015. Spine growth and seismogenic faulting at Mt. Unzen, Japan. J. Geophys. Res. 120, 4034–4054.

Horwell, C.J., Williamson, B.J., Llewellin, E.W., Damby, D.E., Le Blond, J.S., 2013. The nature and formation of cristobalite at the Soufrière Hills volcano, Montserrat: implications for the petrology and stability of silicic lava domes. Bull. Volcanol. 75:696. http://dx.doi.org/10.1007/s00445-013-0696-3.

Hurwitz, S., Christiansen, L.B., Hsieh, P.A., 2007. Hydrothermal fluid flow and deformation in large calderas: inferences from numerical simulations. J. Geophys. Res. 112, B02206. http://dx.doi.org/10.1029/2006JB004689.

Iverson, R.M., Dzurisin, D., Gardner, C.A., Gerlach, T.M., La Husen, R.G., Lisowski, M., Major, J.J., Malone, S.D., Messerich, J.A., Moran, S.C., Pallister, J.S., Qamar, A.I., Schilling, S.P., Vallance, J.W., 2006. Dynamics of seismogenic volcanic extrusion at Mount St. Helens in 2004-2005. Nature 444, 439–443.

Keating, B.H., McGuire, W.J., 2000. Island edifice failures and associated tsunami hazards. Pure Appl. Geophys. 157, 899–955.

Kendrick, J.E., Lavallée, Y., Ferk, A., Perugini, D., Leonhardt, R., Dingwell, D.B., 2012. Extreme frictional processes in the volcanic conduit of Mount St. Helens (USA) during the 2004–2008 eruption. J. Struct. Geol. 38, 61–76.

Kendrick, J.E., Smith, R., Sammonds, P., Meredith, P.G., Dainty, M., Pallister, J.S., 2013. The influence of thermal and cyclic stressing on the strength of rocks from Mount St. Helens, Washington. Bull. Volcanol. 75:728. http://dx.doi.org/10.1007/s00445-013-0728-z.

Kendrick, J.E., Lavallée, Y., Hirose, T., Di Toro, G., Hornby, A.J., De Angelis, S., Dingwell, D.B., 2014. Volcanic drumbeat seismicity caused by stick-slip motion and magmatic frictional melting. Nat. Geosci. http://dx.doi.org/10.1038/ngeo2146.

Kennedy, B., Wadsworth, F.B., Vasseur, J., Schipper, C.I., Jellinek, A.M., von Aulock, F.W., Hess, K.-U., Russell, J.K., Lavallée, Y., Nichols, A.R.L., Dingwell, D.B., 2015. Surface tension driven processes densify and retain permeability in magma and lava. Earth Planet. Sci. Lett. 433, 116–124.

Kennedy, L.A., Russell, J.K., Nelles, E., 2009. Origins of Mount St. Helens cataclasites: experimental insights. Am. Mineral. 94, 995–1004.

Kennedy, L.A., Russell, J.K., 2012. Cataclastic production of volcanic ash at Mount Saint Helens. Phys. Chem. Earth 45-46, 40–49.

Klug, C., Cashman, K.V., 1996. Permeability development in vesiculating magmas: implications for fragmentation. Bull. Volcanol. 58, 87–100.

Kranz, R., Harris, W.J., Carter, N.L., 1982. Static fatigue of granite at 200 °C. Geophys. Res. Lett. 9, 1–4.

Kueppers, U., Scheu, B., Spieler, O., Dingwell, D.B., 2005. Field-based density measurements as tool to identify preeruption dome structure: set-up and first results from Unzen volcano, Japan. J. Volcanol. Geotherm. Res. 141, 65–75.

Kushnir, A.R.L., Martel, C., Bourdier, J.-L., Heap, M.J., Reuschlé, T., Erdmann, S., Komorowski, J.C., Cholik, N., 2016. Probing permeability and microtexture: unravelling the role of a low-permeability dome on the explosivity of Merapi (Indonesia). J. Volcanol. Geotherm. Res. 316, 56–71.

Lagmay, A.M.F., van Wyk de Vries, B., Kerle, N., Pyle, D.M., 2000. Volcano instability induced by strike-slip faulting. Bull. Volcanol. 62, 331–346.

Lamb, O.D., De Angelis, S., Umakoshi, K.H., Hornby, A.J., Kendrick, J.E., Lavallée, Y., 2015. Repetitive fracturing during spine extrusion at Unzen volcano, Japan. Solid Earth 6, 1277–1293.

Lavallée, Y., Varley, N., Alatorre-Ibargüengoitia, M.A., Hess, K.-U., Kueppers, U., Mueller, S., Richard, D., Scheu, B., Spieler, O., Dingwell, D.B., 2012. Magmatic architecture of dome-building eruptions at Volcán de Colima, Mexico. Bull. Volcanol. 74, 249–260.

Lavallée, Y., Benson, P.M., Heap, M.J., Hess, K.-U., Flaws, A., Schillinger, B., Meredith, P.G., Dingwell, D.B., 2013. Reconstructing magma failure and the degassing network of dome-building eruptions. Geology 41, 515–518.

Lesher, C.E., Spera, F.J., 2015. Thermodynamic and transport properties of silicate melts and magma. In: Sigurdsson, H., Houghton, B., McNutt, S.R., Rymer, H., Stix, J. (Eds.), The Encyclopedia of Volcanoes 113-141. Elsevier Academic Press.

Lipman, P.W., Mullineaux, D.R., 1981. The 1980 eruptions of Mount St. Helens, Washington, No. 1250. US Dept. of the Interior, US Geological Survey.

Loaiza, S., Fortin, J., Schubnel, A., Guéguen, Y., Vinciguerra, S., Moreira, M., 2012. Mechanical behavior and localized failure modes in a porous basalt from the Azores. Geophys. Res. Lett. 39. http://dx.doi.org/10.1029/2012GL053218.

Lockner, D., 1993. The role of acoustic emission in the study of rock fracture. Int. J. Rock Mech. Min. Sci. Geomech. Abstr. 30, 883–889.

Marsh, B.D., 1988. Crystal size distribution (CSD) in rocks and the kinetics and dynamics of crystallization. Contrib. Mineral. Petrol. 99, 277–297.

McGuire, W.J., 1996. Volcano instability: a review of contemporary themes. Geol. Soc. Lond. 110, 1–23.

Melnik, O., Sparks, R.S.J., 2002. Dyanmics of magma ascent and lava extrusion at Soufrière Hills Volcano, Montserrat. In: Druitt, T.H., Kokelaar, B.P. (Eds.), The Eruption of Soufrière Hills Volcano, Montserrat, From 1995 to 1999, Geological Society of London, Memoirs. 21, pp. 153–171 London.

Menéndez, B., Zhu, W., Wong, T.-f., 1996. Micromechanics of brittle faulting and cataclastic flow in Berea sandstone. J. Struct. Geol. 18, 1–16.

Nakada, S., Shimizu, H., Ohta, K., 1999. Overview of the 1990–1995 eruption at Unzen volcano. J. Volcanol. Geotherm. Res. 89, 1–22.

Neuman, S.P., 1994. Generalized scaling of permeabilities: validation and effect of support scale. Geophys. Res. Lett. 21, 349–352.

Odbert, H.M., Taisne, B., Gottsmann, J., 2015. Deposit loading and its effect on co-eruptive volcano deformation. Earth Planet. Sci. Lett. 413, 186–196.

Pallister, J.S., Thornber, C.R., Cashman, K.V., Clynne, M.A., Lower, H.A., Brownfield, I.K., Meeker, G.P., 2008. Petrology of the 2004–2006 Mount St. Helens lava dome- implications for magmatic plumbing, explosivity, and eruption triggering. In: Sherrod, D.R., Scott, W.E., Stauffer, P.H. (Eds.), A Volcano Rekindled: The First Years of Renewed Eruption at Mount St. Helens 2004–2006, U.S. Geological Survey Professional Paper 2007-XXXX.

Pallister, J.S., Cashman, K.V., Hagstrum, J.T., Beeler, N.M., Moran, S.C., Denlinger, R.P., 2013. Faulting within the Mount St. Helens conduit and implications for volcanic earthquakes. Geol. Soc. Am. Bull. http://dx.doi.org/10.1130/B30716.1.

Paterson, M.S., Wong, T.-F., 2005. Experimental Rock Deformation - The Brittle Field. Springer, New York 978-3-540-26339-5.

Pola, A., Crosta, G.B., Fusi, N., Barberini, V., Norini, G., 2012. Influence of alteration on physical properties of volcanic rocks. Tectonophysics 566-567, 67–86.

Quane, S.L., Russell, J.K.R., Kennedy, L., 2004. A low-load, high-temperature deformation apparatus for volcanological studies. Am. Mineral. 89, 873–877.

Reid, M.E., 2004. Massive collapse of volcano edifices triggered by hydrothermal pressurization. Geology 32, 373–376.

Rotonda, T., Verrucci, L., Tommasi, P., 2014. Experimental relationships among strength parameters in monoaxial loading conditions for porous effusive rocks. In: Alejano, L.R., Perucho, A., Olalla, C., Jiménez, R. (Eds.), Rock Engineering and Rock Mechanics: Structures in and on Rock Masses. CRC Press. ISBN: 978-1-138-00149-7.

Rust, A.C., Cashman, K.V., Wallace, P.J., 2004. Magma degassing buffered by vapor flow through brecciated conduit margins. Geology 32, 349–352.

Rutherford, M.J., Hill, P.M., 1993. Magma ascent rates from amphibole breakdown: an experimental study applied to the 1980–1986 Mount St. Helens eruptions. J. Geophys. Res. 98, 19667–19685.

Rutter, E., 1986. On the nomenclature of mode of failure transitions in rocks. Tectonophysics 122, 381–387.

Rutter, E., Casey, M., Burlini, L., 1994. Preferred crystallographic orientation development during the plastic and superplastic flow of calcite rocks. J. Struct. Geol. 16, 1431–1446.

Sammis, C.G., Ashby, M.F., 1986. The failure of brittle porous solids under compressive stress states. Acta Metall. 34:511–526. http://dx.doi.org/10.1016/0001-6160(86)90087-8.

Schaefer, L.N., Kendrick, J.E., Oommen, T., Lavallée, Y., Chigna, G., 2015. Geomechanical rock properties of a basaltic volcano. Front. Earth Sci. 3:29. http://dx.doi.org/10.3389/feart.2015.00029.

Scheu, B., Kueppers, U., Mueller, S., Spieler, O., Dingwell, D.B., 2008. Experimental volcanology on eruptive products of Unzen volcano. J. Volcanol. Geotherm. Res. 175, 110–119.

Schultz, R.A., 1996. Relative scale and the strength and deformability of rock masses. J. Struct. Geol. 18, 1139–1149.

Shea, T., Houghton, B.F., Gurioli, L., Cashman, K.V., Hammer, J.E., Hobden, B.J., 2010. Textural studies of vesicles in volcanic rocks: an integrated methodology. J. Volcanol. Geotherm. Res. 190, 271–289.

Siebert, L., 1996. Hazards of large volcanic debris avalanches and associated eruptive phenomena. Monitoring and Mitigation of Volcano Hazards. Springer, Berlin Heidelberg, pp. 541–572.

Shimada, M., 1986. Mechanism of deformation in a dry porous basalt at high pressures. Tectonophysics 121, 153–173.

Siratovich, P.A., Heap, M.J., Villeneuve, M.C., Cole, J.W., Kennedy, B.M., Davidson, J., Reuschlé, T., 2016. Mechanical behaviour of the Rotokawa Andesites (New Zealand): insight into permeability evolution and stress-induced behaviour in an actively utilised geothermal reservoir. Geothermics 64, 163–179.

Smith, R., Sammonds, P.R., Kilburn, C.R.J., 2009. Fracturing of volcanic systems: experimental insights into pre-eruptive conditions. Earth Planet. Sci. Lett. 280 (221-219).

Smith, R., Sammonds, P., Tuffen, H., Meredith, P.G., 2011. Evolution of the mechanics of the 2004–2008 Mt. St. Helens lava dome with time and temperature. Earth Planet. Sci. Lett. 307, 191–200.

Sparks, R.S.J., Murphy, M.D., Lejeune, A.M., Watts, R.B., Barclay, J., Young, S.R., 2000. Control on the emplacement of the andesite lava dome of the Soufriere Hills volcano, Montserrat by degassing induced crystallization. Terra Nova 12, 14–20.

Swanson, D.A., Holcomb, R.T., 1990. Regularities in growth of the Mount St. Helens dacite dome, 1980–1986. Lava Flows and Domes. Springer, Berlin Heidelberg.

Thomas, M.E., Petford, N., Bromhead, E.N., 2004. Volcanic rock-mass properties from Snowdonia and Tenerife: implications for volcano edifice strength. J. Geol. Soc. Lond. 161, 1–8.

Todesco, M., Rinaldi, A.P., Bonforte, A., 2010. Modeling of unrest signals in heterogeneous hydrothermal systems. J. Geophys. Res. 115, B09213. http://dx.doi.org/10.1029/2010JB007474.

Tromans, D., Meech, J.A., 2002. Fracture toughness and surface energies of minerals: theoretical estimates for oxides, sulphides, silicates and halides. Miner. Eng. 15, 1027–1041.

Vallance, J.W., Schneider, D.J., Schilling, S.P., 2008. Growth of the 2004–2006 lava-dome complex at Mount St. Helens, Washington. US Geol. Surv. Prof. Pap. 1750, 169–208.

Vasseur, J., Wadsworth, F.B., Lavallée, Y., Hess, K.-U., Dingwell, D.B., 2013. Volcanic sintering: timescales of viscous densification and strength recovery. Geophys. Res. Lett. 40, 5658–5664.

Violay, M., Gibert, B., Mainprice, D., Evans, B., Dautria, J.-M., Azias, P., Pezard, P., 2012. An experimental study of the brittle-ductile transition of basalt at oceanic crust pressure and temperature conditions. J. Geophys. Res. 117:B3. http://dx.doi.org/10.1029/2011JB008884.

Violay, M., Gibert, B., Mainprice, D., Burg, J.-P., 2015. Brittle versus ductile deformation as the main control of the deep fluid circulation in oceanic crust. Geophys. Res. Lett. http://dx.doi.org/10.1002/2015GL063437.

Voight, B., Elsworth, D., 1997. Failure of volcano slopes. Geotechnique 47, 1–31.

Voight, B., 2000. Structural stability of andesite volcanoes and lava domes. Philosophical Transactions: Mathematical, Physical and Engineering Sciences, 358, No. 1770, Causes and Consequences of Eruptions of Andesite Volcanoes (May 15, 2000), pp. 1663–1703.

Voight, B., Komorowski, J.C., Norton, G.E., Belousov, A.B., Belousova, M., Boudon, G., Francis, P.W., Franz, W., Heinrich, P., Sparks, R.S.J., Young, S.R., 2002. The 26 December (Boxing Day) 1997 sector collapse and debris avalanche at Soufriere Hills Volcano, Montserrat. In: Druitt, T.H., Kokelaar, B.P. (Eds.), The Eruption of Soufriere Hills Volcano, Montserrat, From 1995 to 1999. Geological Society of London, London.

Watters, R.J., Zimbelman, D.R., Bowman, S.D., Crowley, J.K., 2000. Rock mass strength assessment and significance to edifice stability, Mount Rainier and Mount Hood, Cascade Range Volcanoes. Pure Appl. Geophys. 157, 957–976.

Watts, R.B., Herd, R.A., Sparks, R.S.J., Young, S.R., 2002. Growth patterns and emplacement of the andesitic lava dome at Soufrière Hills volcano. Montserrat Geological Society, London, Memoirs 2002. 21:pp. 115–152. http://dx.doi.org/10.1144/GSL.MEM.2002.021.01.06.

Wong, T.-f., David, C., Zhu, W., 1997. The transition from brittle faulting to cataclastic flow in porous sandstones: mechanical deformation. J. Geophys. Res. 102, 3009–3025.

Wong, T.-f., Baud, P., 2012. The brittle-ductile transition in porous rock: a review. J. Struct. Geol. 44, 25–53.

Wright, H.M.N., Cashman, K.V., Gottesfeld, E.H., Roberts, J.J., 2009. Pore structure of volcanic clasts: measurements of permeability and electrical conductivity. Earth Planet. Sci. Lett. 280, 93–104.

Wyering, L.D., Villeneuve, M.C., Wallis, I.C., Siratovich, P., Kennedy, B., Gravely, D.M., Cant, J.L., 2014. Mechanical and physical properties of hydrothermally altered rocks, Taupo Volcanic Zone, New Zealand. J. Volcanol. Geotherm. Res. 288, 76–93.

Zhu, W., Baud, P., Wong, T.-F., 2010. Micromechanics of cataclastic pore collapse in limestone. J. Geophys. Res. 115 (B4). http://dx.doi.org/10.1029/2009JB006610.

Zhu, W., Baud, P., Vinciguerra, S., Wong, T.-F., 2011. Micromechanics of brittle faulting and cataclastic flow in Alban Hills tuff. J. Geophys. Res. 116, B06209. http://dx.doi.org/10.1029/2010JB008046.

Zhu, W., Baud, P., Vinciguerra, S., Wong, T.-f., 2016. Micromechanics of brittle faulting and cataclastic flow in Mt. Etna basalt. J. Geophys. Res. http://dx.doi.org/10.1002/2016JB012826.